

Predicting the Radio Continuum - Galaxy Emission in SHARK, the Semi-Analytical Model of Galaxy Formation

Samuel Hansen

under the supervision of

Dr. Claudia Lagos

This thesis is presented in partial fulfilment of the requirements for the Master of Physics (Astrophysics)



THE UNIVERSITY OF
**WESTERN
AUSTRALIA**



International
Centre for
Radio
Astronomy
Research

School of Physics, Mathematics and Computing
The University of Western Australia

Declaration

This is to certify that:

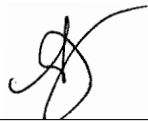
1. This thesis comprises of my original work.
2. Due acknowledgement has been made in the text to all other materials used.
3. This thesis consists of no more than 40 pages inclusive of tables and figures but exclusive of references and appendices.

I authorise the Head of the Department of Physics to make a copy of this thesis to any person judged to have an acceptable reason for access to the information, i.e., for research, study or instruction.

Andrew Sullivan

Student ID: 22466998

Signature:



Date: 17 October 2021.

Chris Power

Signature:



Date: 17 October 2022.

Acknowledgements

I would like to acknowledge that this work has been completed at the University of Western Australia, which is situated on Noongar land, and that the Noongar people remain the spiritual and cultural custodians of this land.

Abstract

TEXT

Contents

1	Introduction	1
1.1	Introduction	1
1.1.1	The Far-Infrared Radio Correlation	1
2	Methods	4
2.1	Methods	4
2.1.1	SHARK	4
2.1.2	Viperfish and ProSpect	6
2.1.3	Free-Free Radiation	9
2.1.4	Synchrotron Emission	11
3	Results	15
3.0.1	Local Universe ($z = 0$)	15
3.0.2	The Distant Universe ($z > 0$)	21
3.0.3	The Far-Infrared Radio Correlation	29
3.0.4	Evolution of q_{IR} with M_*	30
3.0.5	Evolution of q_{IR} with redshift	38
3.0.6	Number Counts	40
4	Discussion	54
4.1	TBD	54
5	Conclusion	55
6	Future Work	56
	References	57
	Appendices	63

Chapter 1

Introduction

1.1 Introduction

1.1.1 The Far-Infrared Radio Correlation

[Planck Collaboration et al. \(2016\)](#) The Far-Infrared Radio Correlation (FIRC) is an observed tight correlation between a population of galaxy's total Far-Infrared (FIR) luminosity and total radio luminosity that spans five orders of magnitude ([Van der Kruit \(1971\)](#), [Van Der Kruit \(1973\)](#), [De Jong et al. \(1985\)](#), [Helou et al. \(1985\)](#), [Condon \(1992\)](#)). It has been shown to exist in a variety of different galactic populations including Sub-Millimetre Galaxies (SMGs) ([Thomson et al. \(2014\)](#), [Algera et al. \(2020\)](#)), (Ultra)-Luminous Infrared Galaxies (ULIRGs) ([Lo Faro et al. \(2015\)](#)), Early Type galaxies ([Omar & Paswan \(2018\)](#)), dwarf galaxies ([Shao et al. \(2018\)](#)), low-ionization nuclear emission-line region (LINERs) and Seyferts ([Solarz et al. \(2019\)](#)), irregular and disk-dominated galaxies ([Pavlović \(2021\)](#)) as well as highly lensed galaxies ([Giulietti et al. \(2022\)](#)), to name a few.

It is often parameterised as it first was in [Helou et al. \(1985\)](#) as in equation ??

$$q_{\text{ir}} = \log_{10} \left(\frac{L_{\text{IR}}}{3.75 \times 10^{12} \text{Wm}^{-2}} \right) - \log_{10} \left(\frac{L_{1.4\text{GHz}}}{\text{Wm}^{-2}\text{Hz}^{-1}} \right), \quad (1.1)$$

where L_{IR} is total FIR integrated over $8 - 1000\mu\text{m}$ in the rest frame and $L_{1.4\text{GHz}}$ the total rest frame radio luminosity at 1.4GHz. While this is the most common parameterisation ([Helou et al. \(1985\)](#), [Condon \(1992\)](#), [Bell \(2003\)](#) etc.) the FIRC has been shown to exist using different frequency combinations as well (ie radio luminosity at 150MHz ([Read et al. \(2018\)](#)), infrared being a combination of $60\mu\text{m}$ and $80\mu\text{m}$ ([Yun et al. \(2001\)](#)) and a variety of different individual infrared frequencies ([Smith et al. \(2014\)](#))).

The FIRC's persistence across different magnitudes of luminosity and varied galactic populations makes it an attractive tool. It's uses include identifying Active Galactic Nuclei (AGNs) ([Donley et al. \(2005\)](#), [Norris et al. \(2006\)](#), [Algera et al. \(2020\)](#)), in defining the SFR-Radio correlation ([Bell \(2003\)](#), [Condon & Ransom \(2016\)](#), [Duncan et al. \(2020\)](#), [Molnár et al. \(2021\)](#)), in determining the distance to SMGs ([Yun & Carilli \(1999\)](#)) and deriving a galaxy's radio emission based on

1. INTRODUCTION

its IR emission (Dale et al. (2014)).

It is therefore important that we totally understand the FIRC and its limitations. In particular understanding any possible evolution the FIRC has with redshift (z). This is a very active area of research into FIRC and has some studies finding that there is some evolution with z (Iverson et al. 2010a,b; Magnelli et al. 2015; Delhaize et al. 2017) and others finding no evolution (Appleton et al. 2004; Jarvis et al. 2010; Sargent et al. 2010a,b; Bourne et al. 2011; Mao et al. 2011; Duncan et al. 2020; Thomson et al. 2014; Algera et al. 2020). Delvecchio et al. (2021) did not find that qir evolved significantly with z , but instead evolved with stellar mass. Reasons that have been suggested for these differences include choice of spectral index (Delhaize et al. (2017)), use of IR or radio biased samples (Sargent et al. (2010b)) and use of statistically insignificant samples (Jarvis et al. (2010)). However the most commonly cited reason is AGN contamination. Even high precision instruments are biased towards high mass and low redshift objects and determining the presence of an AGN in high redshift galaxies is particularly difficult (Delvecchio et al. (2021)).

Despite the wealth of research that has been conducted into the FIRC, our theoretical understanding is quite limited. Fundamentally the FIRC is grounded in star-formation where galaxy's IR and Radio emission come from the same young, massive stars. These stars, formed in dusty, molecular clouds, would emit UV radiation which is subsequently absorbed and re-emitted by these clouds at IR wavelengths. These same stars would ionise HII regions causing free-free emission and when these stars finally die, undergo a core-collapse supernova (CCSN) accelerating cosmic rays as synchrotron radiation (Condon & Ransom (2016)).

However, this simple star-formation model does not account for the FIRC in starbursts. The power of each cosmic ray electron is proportional to the magnetic energy density and hence proportional to the magnetic field of a galaxy. So a powerful starbursting galaxy (with B 1000 μ G) will emit much more powerful cosmic rays than a normal spiral (with B 100 μ G) (Condon & Ransom (2016)). The calorimeter model proposed by Völk (1989) to explain this discrepancy. The assumption is that the lifetime of a cosmic ray electron is proportional to the inverse of the magnetic energy density. Thus, cosmic rays from starbursting galaxies can still be powerful, but only radiate a short time, whereas cosmic rays from normal galaxies at a lower power, but for a proportionally longer time. It's from this understanding of radio emission that Bressan et al. (2002) developed their model for modelling radio emission.

The calorimeter model leads to three assumptions; that galaxies are electron calorimeters, UV calorimeters and that synchrotron radiation is the main loss mechanism. These assumptions are unlikely to be true (Lacki et al. (2010)). Consequently, to explain the FIRC, a number of conspiracies have been suggested. For example Lacki et al. (2010) found that in normal galaxies, when electron calorimetry decreases the radio emission, decreasing UV opacity increases the IR emission. For starbursts, Lacki et al. (2010) found that bremsstrahlung, ionization, and IC losses decrease the synchrotron emission, but this is balanced by secondary electrons and the fact that 1.4GHz observation probe lower cosmic ray energies when magnetic field strength increases. In another conspiracy, Bell (2003) found that IR and Radio are not proportional to

the SFR of a galaxy, but they are disproportional to SFR in complimentary ways that cancel each other out.

With the invocation of uncomfortably well-tuned parameters and potential for new physics it is not surprising that the FIRC has enticed a wealth of studies. This has included some models that have ranged from one-zone model of cosmic ray injection (Lacki et al. (2010)), a 1D model of turbulent clumpy star-forming galactic disks (Vollmer et al. (2022)) and a semi-analytic model (SAM) of a single, idealised galaxy (Schober et al. (2022)). In this paper we use SHARK, a semi-analytic model of galaxy formation to model the FIRC without invoking any conspiracy. As far as we can assess, there is no other model of galaxy formation that also models the FIRC. This makes SHARK the first to directly model a large population of galaxies over cosmic time to include L_{IR} , L_{rad} and consequently qir.

Chapter 2

Methods

2.1 Methods

In this model, we model radio emission as two parts: Free-Free emission and synchrotron emission.

2.1.1 SHARK

SHARK is an open source, semi-analytic model of galaxy formation first presented in [Lagos et al. \(2018\)](#). In this paper we use SHARK v1.1 which is the same presented in [Lagos et al. \(2018\)](#). This version uses the Synthetic Universe For Surveys (SURFS) simulation suite ([Elahi et al. 2018](#)), specifically the L210N1536 simulation, which uses a Λ CDM ([Planck Collaboration et al. 2016](#)) cosmology. That is a Hubble constant of $H_0 = h \times 100(\text{km/s})/\text{Mpc}$, $h = 0.6751$, matter density of $\Omega_m = 0.3121$, baryon density $\Omega_b = 0.0491$ and dark energy density of $\Omega_\Lambda = 0.6879$. The SURFS L210N1536 simulation has a boxsize of $L_{\text{box}} = 210\text{cMpc}/h$ and a softening length $\epsilon = 4.5\text{ckpc}/h$. Each box contains $N_p = 1536^3$ dark matter particles each with a mass of $m_p = 2.21 \times 10^8 M_\odot/h$. The SURFS simulation suite allows for studies of galaxies with stellar masses above $10^7 M_\odot$. This simulation produces 200 snapshots logarithmically arranged from $z = 24 - 0$. This corresponds to a time between snapshots of $\approx 6 - 80\text{Myr}$.

Halos, subhalos and their properties are identified using VELOCIRAPTOR ([Elahi et al. 2019a](#), [Cañas et al. 2019](#)). VELOCIRAPTOR first identifies halos using a 3D friend-of-friend (FOF) algorithm. It also applies a 6D FOF with velocity dispersion to remove spuriously linked objects (like early stage mergers). This 3D FOF structure corresponds to the halo. It then identifies particles that have a local velocity distribution significantly different from the smooth background halo. It runs a phase-space FOF on these particles to identify the subhalos. SURFS only considers halos with $/rm \geq 20$ dark matter particles.

Merger trees are then constructed using TREEFROG ([Elahi et al. 2019b](#)). At its most basic, TREEFROG is a particle correlator that relies on particle IDs being continuous across snapshots. The merger tree is constructed forward in time, identifying the optimum link between progenitors and descendants. TREEFROG searches up to four snapshots to identify optimal links.

VELOCIRAPTOR and TREEFROG provide the subhalo and merger tree catalogues, respectively, which provide the basis from which galaxies are evolved. SHARK evolves these galaxies across snapshots using a physical model. The physical model used here is fully described by equations 49-64 in Lagos et al. (2018). Before this evolution takes place, the merger trees undergo a post processing treatment.

First 'interpolated' subhalos are inserted between snapshots of the current subhalo and its descendants. This interpolated subhalo has the same properties as the progenitor subhalo. This ensures continuity of galaxy evolution across snapshots. Since TREEFROG searches up to four snapshots for primary links, it is possible that a descendant subhalo is not present in the following snapshot, thus causing discontinuity. The interpolated subhalos solve this problem and enforces continuity of galaxy formation.

Second, the merger tree is checked to make sure that the mass of each halo is strictly equal to larger than the halo mass of its most massive progenitor. This ensures a matter accretion rate onto halos is always ≥ 0 .

Third, the central subhalos are found. At the $z = 0$ snapshot, the most massive subhalo of every existing halo is defined as the central subhalo. The main progenitor of this central subhalo is then defined as the central subhalo of their respective halos in the next snapshot and so on back through time. Other subhalos that are not the main progenitor or the most massive subhalo of an existing halo are designated satellite subhalos.

Finally, halos that first appear in the catalogue (the ones without a progenitor) are identified. The central subhalo of this halo is assigned a halo gas reservoir of mass $\Omega_b/\Omega_m \times M_{\text{halo}}$ (where M_{halo} is the mass of the halo). Gas cooling is ignited when halo gas mass is > 0 , and so a cold gas disk is formed. After each snapshot, the galaxies that are hosted by a subhalo are transferred to their descendants and evolved. If a halo is formed without a progenitor and is a satellite subhalo it is defined as a dark subhalo, is not assigned any gas and does not evolve.

Within SHARK there are three different types of galaxies; Centrals, which are the central galaxy of the central subhalo, Satellites, which are the central galaxy of satellite subhalos and Orphans, which are the central galaxy of a defunct subhalo. A defunct subhalo is one which has merged onto another subhalo and is not the main progenitor. From these definitions a central subhalo can have only one central galaxy, but many orphan galaxies, but a satellite subhalo can only have one satellite galaxies.

In this paper we scale up the total volume of each snapshot by utilising 64 independent sub-volumes. Each sub-volume is a box with $V_{\text{box}} = 210^3 [\text{cMpc}/h]^3$ independently evolved from other sub-volumes. This means the total volume under consideration is $V_{\text{total}} = 64 \times 210^3 [\text{cMpc}/h]^3$ in this paper. By increasing the volume, and therefore number of galaxies, being considered we can construct a more robust population of galaxies from which to derive properties. SHARK uses the universal Chabrier IMF (Chabrier 2003).

2. METHODS

2.1.2 Viperfish and ProSpect

This work builds on the galaxy emission models presented in [Lagos et al. \(2019\)](#). This includes using the Spectral Energy Distribution (SED) created for FIR-FUV emission of SHARK galaxies. These SEDs are created using PROSPECT ([Robotham et al. 2020](#)) and VIPERFISH ([Lagos et al. 2019](#)).

PROSPECT is a generative SED package that allows for the creation of SEDs from known star formation and metallicity histories. It can also be used to fit observed SEDs. VIPERFISH is an intermediary tool that connects SHARK with PROSPECT. VIPERFISH extracts star formation histories (SFH) and metallicity formation histories (ZFH) from SHARK and translates them to PROSPECT for SED generation.

PROSPECT was designed to be user friendly with high levels of flexibility in the SFH and ZFH inputs. PROSPECT can make use of the [Bruzual & Charlot \(2003\)](#) or [Vazdekis et al. \(2016\)](#) stellar synthesis libraries and uses a [Chabrier \(2003\)](#) IMF for both libraries. This gives PROSPECT a broad spectral range available for SED generation from stellar synthesis library that is well understood by the astrophysics community. In this paper we use the [Bruzual & Charlot \(2003\)](#) stellar synthesis library and the [Chabrier \(2003\)](#) IMF. This is the same stellar synthesis library used to produce SEDs in [Lagos et al. \(2019\)](#) and the same IMF used in SHARK ([Lagos et al. 2018](#)).

PROSPECT's flexibility in its SFH and ZFH inputs makes it ideal for use with SHARK. In PROSPECT, SFH and ZFH can be arbitrarily complex; internal interpolation schemes map the provided inputs onto the discrete library of temporal evolution available. Note that if the timesteps within the provided ZFH and SFH are too large this can lead to large uncertainties in the resulting emission, particularly UV. In SHARK, the UV emission is accurately predicted as the time-steps are sufficiently fine ([Lagos et al. 2019](#)).

PROSPECT generates SEDs from SHARK by using a simplified fiducial model of dust processing. The light is first attenuated by the [Charlot & Fall \(2000\)](#) dust model. The dust is assumed to be in two phases; birth clouds (BC) and diffuse ISM. The absorption curves for the BCs and ISM are defined in Equations 2.1 and 2.2.

$$\tau_{\text{ISM}} = \hat{\tau}_{\text{ISM}}(\lambda/5500\text{\AA})^{\eta_{\text{ISM}}}, \quad (2.1)$$

$$\tau_{\text{BC}} = \tau_{\text{ISM}} + \hat{\tau}_{\text{BC}}(\lambda/5500\text{\AA})^{\eta_{\text{BC}}}, \quad (2.2)$$

where τ_{BC} and τ_{ISM} are the optical depths at 5500Å for BC and the diffuse ISM respectively, τ_{BC} and τ_{ISM} are the attenuation due to BC and ISM respectively. η_{ISM} and η_{BC} are the spectral slopes for the two attenuation curves.

Light from different stellar age populations are attenuated by dust differently. Birth clouds contain stellar populations younger than 10 Myr and older stars are not present in birth clouds. Hence, light from younger stars has its light attenuated by both Eqns 2.1 and 2.2 while older

stars are only attenuated by Eqn 2.2.

For the calculation of τ_{ISM} , τ_{BC} and η_{ISM} it is necessary to calculate the surface density of dust (Σ_{dust}). In SHARK the calculation of Σ_{dust} is done separately for disks and bulges. For disks the average Σ_{dust} is given by:

$$\Sigma_{\text{dust,disk}} = \frac{M_{\text{dust,disk}}}{2\pi r_{50,d} l_{50}} \quad (2.3)$$

where $M_{\text{dust,disk}}$ is the dust mass in the disk, $r_{50,d}$ is the half-gas mass radius of the disk (both of these quantities are outputs in the HDF5 file from SHARK) and l_{50} is the projected minor axis. Here $l_{50} = \sin(i) * (r_{50,d} - r_{50,d}/7.3)$ where i is the inclination. 7.3 is the scaleheight to scalelength observed relation in local galaxy disks (Kregel et al. 2002). A galaxy's inclination is determined by the host subhalo angular momentum vector or is randomly chosen for orphan galaxies (Chauhan et al. 2019).

For bulges the average Σ_{dust} is given by:

$$\Sigma_{\text{dust,bulge}} = \frac{M_{\text{dust,bulge}}}{2\pi r_{50,d}^2} \quad (2.4)$$

where $M_{\text{dust,bulge}}$ is the dust mass in the bulge and $r_{50,b}$ is the half mass radius of the bulge. Inclination is not important in bulges because we assume they are spherically symmetric.

For attenuation due to the diffuse ISM, Lagos et al. (2019) use the work of Trayford et al. (2017) and Trayford et al. (2019).

Trayford et al. (2017) computed the attenuation for each galaxy in the EAGLE hydrodynamical simulation suite using SKIRT (a software package that can be used for simulating radiation transfer in galaxies). These curves were later parameterised to the Charlot & Fall (2000) model (Trayford et al. 2019). From these parameterised curves the median and $1 - \sigma$ relationship between τ_{ISM} , η_{ISM} and Σ_{dust} were derived. Using these parameterised curves and the Σ_{dust} from SHARK as calculated in Eqns 2.3 and 2.4 τ_{ISM} and η_{ISM} are calculated. These values are then perturbed by sampling from a gaussian distribution with width σ , where σ is the 16th – 84th percentile as predicted by Trayford et al. (2019).

Lagos et al. (2019) follows the Lacey et al. (2016) model for birth cloud attenuation. This model assumes that the birthcloud optical depth scales with the gas metallicity and gas surface density of the cloud, but substitutes the metal surface density with dust surface density of the clouds:

$$\tau_{\text{BC}} = \tau_{\text{BC},0} \left(\frac{f_{\text{dust}} Z_{\text{gas}} \Sigma_{\text{gas,cl}}}{f_{\text{dust,MW}} Z_{\odot} \Sigma_{\text{MW,cl}}} \right) \quad (2.5)$$

where $f_{\text{dust}} = M_{\text{dust}}/M_Z$, (dust-to-metal mass ratio), $\tau_{\text{BC},0} = 1$, $\Sigma_{\text{MW,cl}} = 85 M_{\odot} \text{pc}^{-2}$, $Z_{\odot} = 0.0189$ and $f_{\text{dust,MW}} = 0.33$ so that a typical spirial galaxy, $\tau_{\text{BC}} \approx \tau_{\text{BC},0}$ (matching the result from Charlot & Fall (2000) and Kreckel et al. (2013)).

The cloud surface density is $\Sigma_{\text{gas,cl}} = \max[\Sigma_{\text{MW,cl}}, \Sigma_{\text{gas}}]$ where Σ_{gas} is found using Eqs. 2.3 and 2.4. Galaxies in the local group have a giant molecular cloud with constant gas surface

2. METHODS

density close to the value of $\Sigma_{MW,cl}$ (Krumholz 2014). This gas surface density is independent of galactic environment and has been found in galaxies ranging from metal-poor dwarfs to molecule-rich spirals. Outside of the local group, the giant molecular cloud surface density increases to maintain equilibrium pressure with increasing ISM pressure. Thus, $\Sigma_{gas,cl} \approx \Sigma_{gas}$ in these environments (Krumholz et al. 2009). A physical limit of $\tau_{BC} \geq \tau_{ISM}$. For birth clouds, Lagos et al. (2019) adopts $\eta_{BC} = -0.7$, being the default value from Charlot & Fall (2000). Once the light has been attenuated by the dust model, it must be re-emitted at longer wavelengths. To do this, PROSPECT adopts the empirical templates from Dale et al. (2014) (henceforth the Dale model).

The Dale model has been in development since 2001 and consists of observationally constrained templates to model the complete SED of normal star-forming galaxies (SFG). It is an empirical model largely based on the observations of the local Universe and was initially developed for SFGs and only for the infrared SED (between $3 - 1,100\mu m$ Dale et al. (2001). Based largely on the work of Désert et al. (1990), the Dale model combines the contributions to the SED from large dust grains, very small dust grains and polycyclic aromatic hydrocarbons (PAH) heated by radiation fields of intensity U , with U having a range of $0.3 - 10^5$. Here U measure multiples of the local interstellar radiation field in the Solar Neighborhood; $U = 1$ corresponds to the local interstellar radiation field in the Solar Neighborhood.

The Dale model adopts the same large dust grain emission profile as Désert et al. (1990) using greybody emission, the amplitude and wavelength of which varies with U . For very small dust grains the Dale model combines the result of Draine & Anderson (1985) and Tran et al. (2001). Draine & Anderson (1985) found the temperature distribution for a variety of graphite grain sizes. They showed that graphite grains of size $0.02\mu m$ will radiate at a single temperature around 20K, smaller graphite grains will radiate over much larger temperature ranges. However, this was only done for a small range of heating intensities. Tran et al. (2001) showed that small dust grain temperature distribution profiles are equivalent to temperature distribution profiles of larger grains. The Dale model combines these two results and employs the approach from Désert et al. (1990) of integration of flux normalisation of the very small grain emission curves to construct very small dust grain profiles for $U = 0.3 - 10^5$.

For PAH's, the Dale model adopts the PAH spectrum model from Désert et al. (1990), but inserts splices of observed mid-IR spectrum from their own observations made using the Infrared Astronomical Satellite (IRAS) and ISOCAM broadband observations. These are further scaled by integrating over the $12\mu m$ IRAS filter, to construct the emission curve for PAH's.

The large dust grain, very small dust grain and PAH emission profiles are then superimposed upon each other using relative contribution ratio of 64:4.7:4.3 (large dust grains: very small dust grains: PAHs) as per Désert et al. (1990). This results in what is referred to as a 'local' SEDs: synthetic SEDs for a range of dusty environments.

In order to construct a 'global' SED or that of a galaxy the Dale model assumes a power-law

distribution in a given galaxy of dust mass over heating intensity:

$$dM_d(U) \propto U^{-\alpha} dU, 0.3 \leq U \leq 10^5, \quad (2.6)$$

where $dM_d(U)$ is the dust mass heated by a radiation field intensity U and α represents the relative contributions of different local SEDs. By convolving this semi-empirical model with Infrared Space Observatory (ISO) and IRAS broadband filter bandpasses, [Dale et al. \(2001\)](#) was able to reproduce the SED of galaxies observed using ISO and IRAS in the infrared.

For the generation of SEDs using PROSPECT, we adopt an $\alpha = 3$ for the diffuse ISM and $\alpha = 1$ for birthclouds. These values approximately correspond to effective dust temperatures of 20 – 25K for the ISM and 50 – 60K for birth clouds. We also assumed no AGN emission is present (which is left for future work).

By adding the attenuated stellar light with the dust emission together we can create the full generative spectrum. This observed frame is then redshifted using the full spectral resolution available. The spectrum is then passed through a number of filters to span the FUV to FIR for the final outputs. These results do not include nebular emission lines and is only based on broad band emission.

In the 2014 update to the Dale model ([Dale et al. 2014](#)), the radio part of the SED was added meaning that the Dale model spans from infrared to the radio spectrum. This means that it is possible to create an SED of a star forming galaxy (SFG) from the infrared to the radio using VIPERFISH and PROSPECT as described above. This extension was implemented using the infrared-radio correlation (q_{IR}). By assuming a constant q_{IR} , it is trivial to find the corresponding radio luminosity from a given infrared luminosity. However, assuming a constant q_{IR} is problematic. Recent observational results have brought in to question the rigidity of this constant q_{IR} and later in this paper we show that a constant q_{IR} cannot be assumed for all SFGs. Consequently we utilise a different method of finding the radio spectrum that is independent of the infrared light produced by the Dale model. This method, which we discuss in the next sections, was developed in [Bressan et al. \(2002\)](#) and [Obi et al. \(2017\)](#) and henceforth will be referred to as the B02 and O17 respectively.

2.1.3 Free-Free Radiation

When a particle is accelerated by an electric field, free-free radiation is produced ([Condon \(1992\)](#)). Free-free radiation (also known as thermal emission) occurs where an electron has its path deflected by the presence of another charged particle (it is so called free-free emission since the electron is free before and after the interaction with the particle) ([Condon & Ransom \(2016\)](#)).

We model free-free radiation to be proportional to the production rate of Lyman continuum photons. Lyman continuum photons are those with a wavelength smaller than 921Å which are responsible for completely ionising hydrogen. Young, massive stars produce large amounts of

2. METHODS

Lyman continuum photons which, when incident to the hydrogen gas region surrounding a star completely ionises the hydrogen present. This then leads to an abundance of electrons and positive ions in these regions (known as HII regions or Strömgren Spheres (Strömgren (2013))) hence many electron-ion interactions can take place leading to free-free radiation (Condon & Ransom (2016)). This is the approach used in Bressan et al. (2002) and Obi et al. (2017) which is based on the work of Rubin (1968) and Condon (1992).

The production rate of Lyman continuum photons Q_H is commonly expressed in Eq. 2.7.

$$Q_H = \int_0^{\lambda_0} \left(\frac{\lambda L_\lambda}{hc} \right) d\lambda, \quad (2.7)$$

where λ_0 is the Lyman limit, 921 Å, L_λ is the composite SED of a galaxy in $\text{ergs}^{-1} \text{Å}^{-1}$, h is Planck's constant and c is the speed of light. L_λ is sourced from SEDs created using the PROSPECT and VIPERFISH models as discussed in section 2.1.

Rubin (1968) (henceforth Rubin) was the first to quantify the relation between free-free radiation and the number of Lyman continuum photons. While the proof of which will not be reproduced here, Rubin starts by considering that the production rate of Lyman continuum photons will equal the destruction rate of Lyman continuum photons. Lyman continuum photons are destroyed during the photo-ionisation processes of ionising hydrogen. Rubin combines this creation-destruction equilibrium with the expression for free-free radiation total flux density from Oster (1961) and Mezger & Henderson (1967). A key assumption of the free-free radiation total flux density from Oster (1961) and Mezger & Henderson (1967) is that the frequency is large enough to ignore self-absorption.

This leads to the relation that approximates total flux density of free-free emission as a function of the number of Lyman continuum photons, temperature, frequency and distance. There is also a self-absorption term present in this equation, however as Rubin notes, for most galaxies it is possible to ignore self-absorption.

Condon (1992) would later re-express this approximation to be between luminosity, production rate of Lyman continuum photons, temperature and frequency, which is given in Eq. 2.8,

In this paper, we model Free-Free radiation in the same way as in B02 and O17 in Eq. 2.8. This model is well understood theoretically and was developed by in Rubin (1968) and Condon (1992).

$$\frac{L_{\text{ff}}}{\text{WHz}^{-1}} = \frac{Q_H}{6.3 \times 10^{32} \text{s}^{-1}} \left(\frac{T}{10^4 \text{K}} \right)^{0.45} \left(\frac{\nu}{\text{GHz}} \right)^{-0.1} \quad (2.8)$$

Equation 2.8 is used in this model to calculate the free-free radiation and is identical to that used in O17 (See Equation 5 in that paper). Note that this equation is of the same form of the equation used to model free-free radiation in B02, but uses a different constant in the denominator of the production rate of Lyman continuum photons; B02 and we use $6.3 \times 10^{32} \text{s}^{-1}$ and B02 use $5.495 \times 10^{32} \text{s}^{-1}$. (See Equation 1 in B02). B02 used their own simulation model of HII regions to calculate an average relation at 1.49 GHz to find $5.495 \times 10^{32} \text{s}^{-1}$. In this paper,

we elect to use $6.3 \times 10^{32} \text{s}^{-1}$ since it comes from a purely theoretical understanding of free-free radiation.

We assume a constant temperature of 10^4K which aligns with observations of HII regions (Anderson et al. 2009).

2.1.4 Synchrotron Emission

When a particle is accelerated by a magnetic field magnetobremstrahlung (magnetic braking radiation) is produced (Condon & Ransom (2016)). The characteristic of the radiation produced can change depending on the speed of the electron being accelerated. Electrons travelling at ultra-relativistic speeds produce synchrotron radiation (also known as non-thermal radiation), which can account to up to 90 percent of light from SFGs at radio wavelengths (Condon (1992)). The physics behind synchrotron radiation is not as well understood as free-free radiation. As with free-free emission, we take the approach taken by B02 and O17. Relativistic electrons accelerated by core-collapse supernovae (CCSN) into the ISM is used as the dominant mechanism of synchrotron radiation with a minor contribution from supernova remnants (SNR) also included. Synchrotron radiation is calculated through Eq. 2.9, which identical to equation 17 in B02.

$$\frac{L_{sync}(\nu)}{[10^{23} \text{WHz}^{-1}]} = \left[E^{SNR} \left(\frac{\nu}{1.49 \text{GHz}} \right)^{-0.5} + E^{EI} \left(\frac{\nu}{1.49 \text{GHz}} \right)^{-\alpha} \right] \times \frac{\nu_{CCSN}}{[yr]}, \quad (2.9)$$

where E^{SNR} is the energy contribution from SNR, E^{EI} is the energy of electrons injected per SN event, α , the radio slope from electrons injected per SN event and ν_{CCSN} is the rate of CCSN. In this equation we assume that E^{SNR} , E^{EI} and α are constants and take the values $E^{SNR} = 1.16 \times 10^{22} \text{WHz}^{-1}$, $E^{EI} = 1.82 \times 10^{23} \text{WHz}^{-1}$ and $\alpha = 0.816$. The values these constants take are derived empirically and differ from those used in the B02 and O17; we change the rate of CCSN within the Galaxy to match the IMF of SHARK when deriving these constants. The derivation and assumptions made within remain the same as that in B02. Later in this section, we present the brief derivation of these constants for completeness.

In Equation 2.9 ν_{CCSN} is not assumed to be constant, but instead calculated from the adopted IMF:

$$\frac{\nu_{CCSN}}{[yr^{-1}]} = \frac{\alpha_{CCSN}}{[M_{\odot}^{-1}]} \times \frac{\text{SFR}}{[M_{\odot}/yr]}. \quad (2.10)$$

In this paper, we adapt the model to directly calculate ν_{CCSN} for each galaxy in SHARK. ν_{CCSN} is modelled as directly dependent on the Star-formation rate (SFR) of a galaxy through Equation 2.10 where α_{CCSN} is the fraction of stars that undergo CCSNe per unit solar mass formed.

It is a common assumption that the stars that eventually undergo CCSNe exist within the

2. METHODS

mass range of $8 M_{\odot} \lesssim M \lesssim 50 M_{\odot}$ (Heger et al. (2003), Ando et al. (2003), Nomoto (1984), Tsujimoto et al. (1997)). Above this maximum mass, stars undergo hypernova and causing Gamma Ray Bursts (Van den Heuvel & Yoon 2007). Consequently α_{CCSNe} can be expressed as it is in Equation 2.11 where $\psi(M)$ IMF.

$$\alpha_{CCSNe} = \frac{\int_{8M_{\odot}}^{50M_{\odot}} \psi(M) dM}{\int_{0.1M_{\odot}}^{100M_{\odot}} M \psi(M) dM} \quad (2.11)$$

As discussed in Section 2.1, we use the stellar synthesis library from Bruzual & Charlot (2003) when creating the SEDs using PROSPECT. The Bruzual & Charlot (2003) stellar synthesis library has a mass range of $0.1M_{\odot}$ to $100 M_{\odot}$ (hence the mass range chosen in the denominator of Equation 2.11). Both PROSPECT and the Bruzual & Charlot (2003) stellar synthesis library make use of the Chabrier (2003) IMF, where $A = 0.158 (\log M_{\odot})^{-1} \text{ pc}^{-3}$, $m_c = 0.079$, $\sigma = 0.69$ and $B = 4.43 \times 10^{-2} (\log M_{\odot})^{-1} \text{ pc}^{-3}$.

$$\psi(\log(M)) = \begin{cases} A * e^{[-(\log(M) - \log(m_c))^2 / 2\sigma^2]} & M \leq 1M_{\odot} \\ B * M^{-1.3} & M > 1 \end{cases} \quad (2.12)$$

where $A = 0.158 (\log M_{\odot})^{-1} \text{ pc}^{-3}$, $m_c = 0.079$, $\sigma = 0.69$ and $B = 4.43 \times 10^{-2} (\log M_{\odot})^{-1} \text{ pc}^{-3}$. For a Chabrier (2003) IMF, and using the mass limits above, $\alpha_{CCSNe} = 0.011 M_{\odot}^{-1}$.

The derivation of constants in 2.9 is as follows. The B02 derives the total synchrotron emission in our galaxy using the result of Berkhuijsen (1984). Berkhuijsen (1984) found the total synchrotron radiation observationally from our Galaxy at 408 MHz: $L_{0.408\text{GHz}} = 6.1 \times 10^{21} \text{ WHz}^{-1}$. Assuming a radio slope of $\alpha = 0.8$ we convert this to the total synchrotron luminosity at 1.49 GHz: $L_{1.49\text{GHz}} = 2.13 \times 10^{21} \text{ WHz}^{-1}$. It is possible to then find the average synchrotron luminosity per supernova event, E^{sync} :

$$E^{\text{sync}} = \frac{L_{1.49\text{GHz}}}{\nu_{CCSN,MW}} = 1.24 \times 10^{23} \text{ WHz}^{-1} \quad (2.13)$$

where $\nu_{CCSN,MW}$ is the rate of CCSN in the Milky Way Galaxy. $\nu_{CCSN,MW}$ is assumed to be constant and we take $\nu_{CCSN,MW} = 0.011 \text{ yr}^{-1}$ which is calibrated with the Chabrier IMF used in SHARK. B02 and O17 assumes a $\nu_{CCSN} = 0.015 \text{ yr}^{-1}$ which appears to be from Cappellaro & Turatto (2001) and uses a Salpeter IMF. It is this difference in $\nu_{CCSN,MW}$ that results in the different constants used in this paper than those used in B02 and O17.

An electron's lifetime and the luminosity of a galaxy are both dependent on the magnetic and radiation density fields. Different environments can have differences in these density fields. It is an open question that the FIR/radio correlation is seemingly unaffected by these differences. In order to reconcile this, the Bressan model assumes that the lifetime of synchrotron electrons is much smaller than the fading time of CCSN rate. The Bressan model also assumes that the cosmic ray electrons are injected during the adiabatic phase of SN explosions. On these timescales, the bolometric synchrotron luminosity is

$$L_{bol}^{sync} = \int_0^{\min(T, \tau_s^{el})} \nu_{CCSN}(T-t) l^{sync}(t) dt, \quad (2.14)$$

where t is lookback time, $l^{sync}(t)$ is the synchrotron luminosity of the injected electrons after time t , T is the age of the galaxy and τ_s^{el} is the lifetime of electrons against synchrotron losses. For SFGs, $\tau_s^{el} \ll T$ and the SFR is almost constant over the last Gyr, the intergral can become

$$L_{bol}^{sync} = \nu_{CCSN} \int_0^{\tau_s^{el}} \frac{dE}{dt} dt = \nu_{CCSN} E^{EI} \quad (2.15)$$

where $l^{sync}(t) = \frac{dE}{dt}$. Hence, the bolometric synchrotron luminosity scales linearly with ν_{CCSN} with a constant E^{EI} .

Equation 2.15 can also be extended for starburst galaxies. To avoid losses from inverse Compton scattering, τ_s^{el} must be shorter than that of SFGs (Condon, 1992). On a short time scale, we assume that ν_{CCSN} is constant.

This relation can also be extended to specific luminosities. This is shown in B02 and will not be reproduced here. The critical assumptions is that ν_{CCSN} is constant over electron lifetimes and energy loss is due to synchrotron radiation. B02 also shows that specific luminosity has a very weak dependence on magnetic field and argues that bolometric magnitude has no dependence on magnetic fields. This is because, in integrating from specific to bolometric magnitudes, the limits of integration for frequency match with the limits in energy where the power law electron distribution applies.

The Bressan model also considers the contribution of Supernova Remnants (SNR), noting that other sources provide a negligible contribution. Again we will not reproduce this derivation in detail, but will summarise the key assumptions. Using the surface brightness-diameter (Σ - D) relation from observations made by ??, the authors derive the integrated contribution of a population of SNRs which arise from a burst of instantaneous star formation. Assuming that the lifetime of an SNR is associated with its adiabatic phase (Condon (1992)) and integrating over the past SFR, they then derive the average SNR synchrotron luminosity per SN event to be:

$$E^{SNR} \simeq 0.06 E^{sync}. \quad (2.16)$$

Equation 2.16 tells us that the contribution from SNR makes up about 6 percent of the synchrotron emission. The remaining 94 percent comes from electrons injected into the ISM and accelerated by magnetic fields. As previously derived, $E^{sync} = 1.24 \times 10^{23} \text{WHz}^{-1}$ and so $E^{EI} = 1.25 \times 10^{23} \text{WHz}^{-1}$, $E^{SNR} = 0.0795 \times 10^{23} \text{WHz}^{-1}$.

SNRs have a spectrum which is modelled by $L_\nu = \nu^{\alpha_{SNR}}$ where $\alpha_{SNR} = 0.2 - 0.5$. The Bressan model assumes that the radio slope of SNRs is constant at $\alpha_{SNR} = 0.5$, which is less than the characteristic observed slope of the total non thermal emission of normal galaxies ($\alpha_{sync} = 0.8$). In order to compensate for this, the Bressan model assumes that the spectrum for electrons

2. METHODS

injected into the ISM has a radio slope of $\alpha_{\text{EI}} \simeq 0.9$ for an overall synchrotron radio slope of $\alpha_{\text{sync}} = 0.8$.

We differ in our approach to radio slopes. Like the Bressan model we too assume that $\alpha_{\text{SNR}} = 0.5$ but use a $\alpha_{\text{EI}} = 0.816$ since this more accurately produces an overall slope of $\alpha_{\text{sync}} = 0.8$. Solving Equation ?? gives the result of $\alpha_{\text{EI}} = 0.816$.

Implementing the effects of synchrotron self-absorption was considered, however these effects have been shown to be negligible at the brightness temperatures of SFGs (Condon (1992)). Because of this, we do not include the effects of synchrotron self-absorption in this model.

Chapter 3

Results

3.0.1 Local Universe ($z = 0$)

Comparisons with the GAMA Survey

Figure 3.1 is a comparison plots between the model from SHARK and observational data of individual galaxies. The radio data presented here is sourced from the SFG population from [Davies et al. \(2017\)](#) at 1.4GHz. This data is sourced by combining data from the Galaxy And Mass Assembly (GAMA) survey and the Faint Images of the Radio Sky at Twenty cm (FIRST) survey. The IR data is sourced from the cross-matched catalogue from [Bellstedt et al. \(2020\)](#) which uses data from the fourth data release of the Kilo-Degree Survey (KiDS) using the Very Large Telescope (VLT). For simplicity I shall refer to this data as being from the GAMA survey. This data is mostly from the local Universe with redshifts of $0 \leq z \leq 0.5$.

[Davies et al. \(2017\)](#) uses a robust methodology of removing AGNs from the sample. This methodology is discussed in depth in that paper, but briefly it involves: (i) classifying AGNs using a BPT diagram ([Baldwin et al. 1981](#)), (ii) using a colour selection using Wide-field Infrared Survey Explorer (WISE) to remove dust obscured objects and passive galaxies, (iii) removing radio luminous objects with a rest-frame radio luminosity $\geq 10^{23.5} \text{WHz}^{-1}$, (iv) using the Near Infrared (NIR) to Mid-Infrared (MIR) ratio (NIR/MIR) ([Seymour et al. 2008](#)), (v) those with an r-band effective radius of > 8 arcsec ([Hopkins et al. 2003](#)) and (vi) visually inspecting the spectrum for broad $\text{H}\alpha$ emission and two component radio emission.

This rigorous AGN cleaning process means the final sample is scoured of most AGN contamination. The process described above is helped by the low redshift of these galaxies. The galaxies that have survived the AGN cleaning process are then matched with those from [Bellstedt et al. \(2020\)](#) to find their total IR observations.

This data is then compared with SHARK. Only galaxies defined as SFG (as determined in the process outlined in section XYZ) at $z = 0$ are compared here. This selection closely matches GAMA’s population of galaxies without introduces selection biases. In Figure 3.1, individual GAMA galaxies are shown as dots and the solid blue line represents the median of the SHARK galaxies selected here. The blue area around this line in the left-hand plot shows the $1 - \sigma$

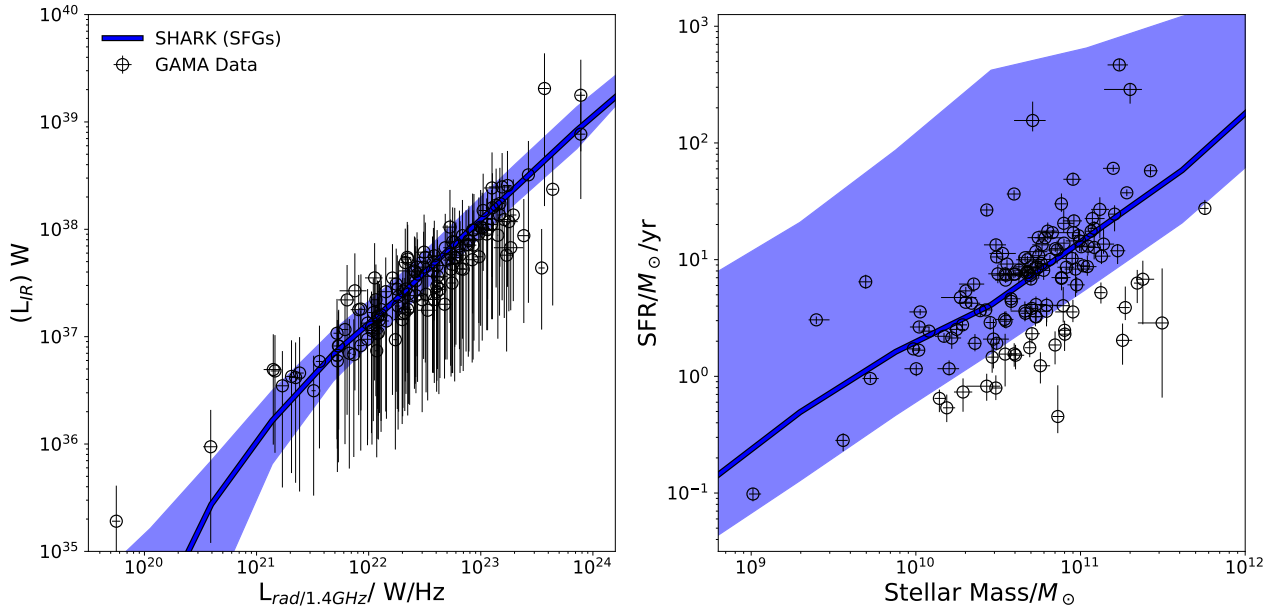


Figure 3.1: Comparison plots with observational data of individual SFGs from the GAMA survey. In both plots, the circles are observational data from the GAMA survey and the blue area is representations from SHARK using our radio model. The left plot shows the L_{IR} vs. $L_{rad}(1.4\text{GHz})$ for these two populations. In this plot, the area in blue around the median line represents $1-\sigma$ uncertainty. The right plot shows SFR vs. total stellar mass where the shaded blue region shows the full extent of the galaxy population, hence the extent of our definition of SFGs. Both plots contain the same galaxies from the GAMA survey and the same subset of galaxies from SHARK. In this subset we have chosen all SFGs at $z = 0$, with the stellar mass range of $8 \leq \log(M/M_{\odot}) \leq 12$ and with a total infrared luminosity greater than 10^{35}W .

values of the SHARK population. In the right plot, the blue area shows the full extent of the population.

One small caveat is that the GAMA data shows individual galaxies, while the SHARK line represents a population of galaxies. It is clear from the Figure 3.1 that there are some galaxies from GAMA that are not within the $1 - \sigma$ value of SHARK. This does not mean that these galaxies have no counterpart in SHARK, just that they appear outside the standard population of SHARK galaxies.

The left panel of Figure 3.1 shows L_{IR} to $L_{\text{Rad}, 1.4\text{GHz}}$. This plot is used to show the FIRC, which is present in both the GAMA and SHARK populations. Both populations agree well with each other with all GAMA galaxies being at least within the margin of error from the median SHARK galaxy at the same L_{rad} .

That the SHARK re-creates the FIRC is not surprising; the model of radio emission depends on it (Bressan et al. 2002). That SHARK re-creates the FIRC in line with independent observations from GAMA is the point here. This is a first confirmation that the radio model used in this paper is reasonable and re-creates observational results.

While the left panel of Figure 3.1 shows a mostly straight line between L_{IR} and $L_{\text{Rad}, 1.4\text{GHz}}$, the median line dips for low luminosity galaxies $L_{\text{Rad}, 1.4\text{GHz}} < 10^{21}$. It is at this point that FIRC appears to break down. This is discussed further in section XYZ of this paper.

The right panel of Figure 3.1 shows the SFR-Stellar Mass plane. This plot is a diagnostic plot showing the veracity of the definition of a SFG used in this paper. This shows that the definition employed here is reasonable, though perhaps a greater definition could have been used. There are some SFGs that appear in GAMA that don't have a counterpart in SHARK and that's due to the restrictive definition employed here. However, overall, it does show that this is a reasonable definition of SFGs.

Radio LFs at $z = 0$

Figure 3.2 shows the radio luminosity function (LF) at $z = 0$ at a frequency of 1.4GHz and 150MHz. The radio LF shows the distribution of galaxies across different bins of luminosity. To find the radio LF I first took a histogram of the \log_{10} radio luminosities of all galaxies at $z = 0$. This histogram is taken over a set of bins with equal bin width. This histogram is then divided by the total volume of the simulation (for all 64 snapshots this is $210\text{Mpc}^3 \times 64$ snapshots) and the bin width of the histogram. The $1 - \sigma$ confidence intervals is then estimated using bootstrapping.

In observations, there can be many sources of error that can affect the results of the radio LF. These can include radio K correction, error in completeness, contamination by AGNs (Novak et al. 2017), cosmic variance (Driver et al. (2022)) and low sample sizes (Bonato et al. (2021b)). In SHARK, no K correction is required (Though we do assume a constant spectral index of $\alpha = -0.8$) and the resolution is clearly complete. No AGNs are modelled in the radio luminosities so contamination cannot occur. Any affect from cosmic variance would be very low

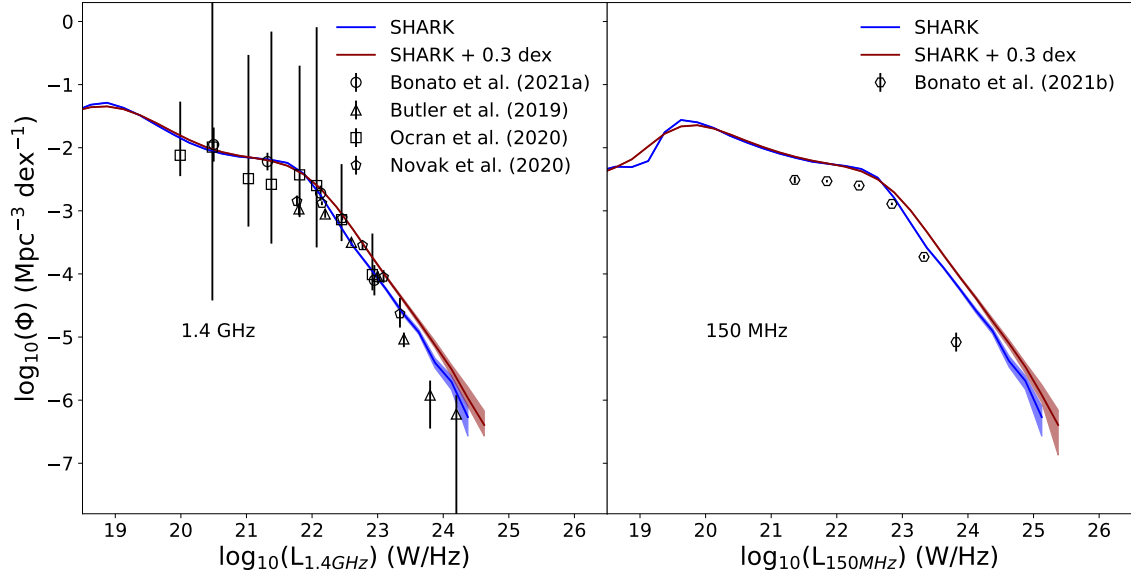


Figure 3.2: The radio LF for all galaxies at $z = 0$ for frequencies 1.4GHz (left) and 150MHz (right). *Left:* The blue line shows the LF with no convolution while the dark red line shows the LF convolved with a Gaussian with a mean of 0 and a standard deviation of 0.3. Errors have been approximated using bootstrapping and the $1 - \sigma$ lines are shown in the shaded regions about the median line. Comparisons are made with observational data of SFGs from [Bonato et al. \(2021a\)](#), [Butler et al. \(2019\)](#) (This data also includes high-excitation sources for which star formation is the likely cause of their radio emission), [Novak et al. \(2017\)](#) and [Ocran et al. \(2019\)](#). *Right:* Same as the left plot except at 150MHz. Comparisons are made with observational data of SFGs from [Bonato et al. \(2021b\)](#).

since the volume of the sample is $13,440 Mpc^3$. Finally, our sample sizes are very large due to the computational ease by which galaxies are modelled.

In order to estimate the effects that the results of these errors can have on the radio LF I convolve the radio LF. During convolution, each individual galaxy luminosity is multiplied by a random constant, before binning. This constant is chosen from a random Gaussian with a mean of 0 and a standard deviation of 0.3. Convoluting luminosities in this way provides an analogue estimation of errors made in observations. This process is the same for both frequencies. The convolved radio LF is shown in red and the non-convolved radio LF is shown in blue.

The result of this is compared with the observational results from [Bonato et al. \(2021a\)](#), [Butler et al. \(2019\)](#), [Novak et al. \(2017\)](#) and [Ocran et al. \(2019\)](#) (for 1.4GHz) and with [Bonato et al. \(2021b\)](#) (for 150MHz). These all show for SFGs, though different methods have been used to determine the presence of AGNs and to quantify the errorbars.

[Bonato et al. \(2021a\)](#) (from which these observational results are sourced) used data from the Westerbork Synthesis Radio Telescope (WSRT) to derive the radio LF. This survey covered an area of $\sim 1.4 \text{ deg}^2$ and to a redshift of $z \sim 3.2$. Radio Loud AGNs are removed using a radio threshold and a radio/SFR threshold. Radio Quiet AGNs are classified using the criterion from [Messias et al. \(2012\)](#). Error bars only show the Poisson error of the sample.

[Butler et al. \(2019\)](#) used the Australia Telescope Compact Array (ATCA) to observe an area of $\sim 25 \text{ deg}^2$ to a redshift of $z \sim 1.3$. AGNs are removed using a decision tree in [Butler et al. \(2018\)](#). This decision tree uses: (i) X-Ray Luminosities and Hardness ratios, (ii) SED fitting, (iii) Mid-Infrared colours, (iv) Optical Spectra, (v) Optical colours and (vi) Radio Luminosities, spectral indices and morphologies to decide whether a source contains an AGN or not. Despite this comprehensive method of AGN cleaning, [Butler et al. \(2018\)](#) acknowledges that AGN contamination is still possible within their data. The error bars here represent the standard deviation of the inverse completeness fraction.

[Novak et al. \(2017\)](#) used the Very Large Array (VLA) covering an area of 2 deg^2 to a redshift of $z \sim 5$. The authors did not remove all AGNs from their sample, rather only radio loud AGNs. The radio loud AGNs were removed with SED fitting. The error bars here are the Poisson error of the sample and does not include errors from radio K correction, sample completeness or radio quiet AGN contamination.

[Ocran et al. \(2019\)](#) used the Giant Meterwave Radio Telescope (GMRT) to measure an area of 1.2 deg^2 , to a redshift $z \sim 5$ at 610MHz. They use the sample from [Ocran et al. \(2020\)](#) and convert to 1.4GHz by assuming a constant spectral index of $\alpha = -0.8$. AGNs are removed using the following diagnostics: (i) a radio cutoff, (ii) the mid-infrared radio ratio, (iii) X-Ray luminosity, (iv) colour-colour diagram and (v) the use of BOSS CLASS and SUB CLASS ([Bolton et al. \(2012\)](#)). Error bars are calculated using confidence tables from [Gehrels \(1986\)](#).

For the 150MHz radio LF, [Bonato et al. \(2021b\)](#) used data from the Low Frequency Array (LOFAR). They use SED fitting to determine AGNs. Error bars are the the quadratic sums of the Poisson uncertainty and sample variance.

At $z = 0$, we find excellent agreement in the radio LF at 1.4GHz. At this frequency, the

3. RESULTS

non-convolved line appears to agree more with the observational data than the convolved line. Notably, this LF was produced without the need to invoke a top-heavy IMF.

Numerous studies into modelling the UV-FIR have required using a top-heavy IMF (that is, an IMF that produces an overabundance of high mass stars) to reproduce observational results. (Baugh et al. 2005; Lacey et al. 2008; Camps et al. 2016; Cowley et al. 2019; Trčka et al. 2020). The exception to this is Lagos et al. (2019), on which this study builds. Lagos et al. (2019) was able to reproduce the UV-FIR LFs using SHARK without invoking a top-heavy IMF. The reasons for this discrepancy between top-heavy and non-top heavy IMF models is discussed in depth in Lagos et al. (2019), but differences in the physical models is the cause of this discrepancy. However as the processes within the physical models are complex and intertwined, a single culprit cannot be found.

This discussion comes with the caveat that as best I can tell, there are no other radio LFs that have been created using SAM except for the SHARK model shown here. It's conceivable that innate differences between the modelling of the UV-FIR LF and the radio LF mean that the UV-FIR is more susceptible to changes in the IMF than the radio. But such discussions stray away from the purpose of this thesis. The overall point is this; the model presented here can successfully reproduce the radio LF at 1.4GHz without invoking a top-heavy IMF.

The right panel of Figure 3.2 shows the radio LF at $z = 0$ for 150MHz . Contrary to the left panel, this does not show good agreement with observational results. The non-convolved model agrees with the points from $22.8 - 23.3$, but over predicts the LF at other points. The convolved line does not predict any of the points at all.

Since the SHARK model is over predicting compared with observations it is possible to rule out two common causes of disagreement: a top-heavy IMF and AGN contamination in the observational data. The reason a top-heavy IMF is invoked in other studies is because they do not have enough high mass stars to reproduce the light. This causes their LF to under predict compared with observations (the opposite of what is seen here). If the discrepancy in the 150MHz LF is caused by the IMF, it would require a top-light IMF (an IMF that produces a scarcity of high mass stars). Further, the IMF is unlikely to be the cause of this discrepancy since the LF is able to be reproduced at 1.4GHz and in UV-FIR in SHARK (Lagos et al., 2019). Further, it is unlikely to be AGN contamination of the data from Bonato et al. (2021b) since SHARK is under predicting compared with the data. AGN contamination causes an increase in the luminosity at radio wavelengths. If AGN contamination were a factor in this data, then SHARK would be underpredicting the data. Also, cleaning data for AGNs is far easier at low redshifts than at high redshifts, meaning that it's more likely that more AGNs have been removed from the low redshift data here than at higher redshifts.

There are two likely causes of this discrepancy: underestimation of error in the Bonato et al. (2021b) data and spectral index used in SHARK. The data from Bonato et al. (2021b) does not include errors due to cosmic variance and low sample sizes, instead using Poisson error (notably, the final point of this data only contains two galaxies). This error is then systemically underestimated in this data set. By including this error it's likely that SHARK would better

agree with the data shown here.

The data from [Bonato et al. \(2021b\)](#) was measured at 150MHz so there is no conversion using spectral index. However the model used in SHARK is calibrated to 1.4GHz and then converts to other frequencies assuming that SFGs follow a power law distribution with a spectral index of $\alpha = -0.8$. While this assumption is widely spread widely in the literature, there are some suggestions that this might not be the case ([Delhaize et al., 2017](#)). Since the observational data appears below the SHARK line, this suggests that the spectral index used in SHARK is not steep enough. If the spectral index used here is the reason for this discrepancy, then it should be reduced.

It is also worth mentioning that as best that I can tell, [Bonato et al. \(2021b\)](#) is the only paper where the RL is found observationally at 150MHz without assuming a spectral index. Other observations are usually done at 1.4GHz and converted to 150MHz by assuming a spectral index. That SHARK disagrees with one source of observational data is neither surprising nor a reason to disregard the SHARK model entirely.

Previous studies have also found discrepancies between observational and modelled LFs due to underestimation of the SFR ([Somerville et al., 2012](#)). This is discussed at length in section XYZ where it is shown not to be the case.

Overall the SHARK RLs agree at 1.4GHz with observations, but do not quite agree at 150MHz. This may be due to many factors including the spectral index used in the SHARK model and the underestimation of error in the observational data.

3.0.2 The Distant Universe ($z > 0$)

Comparisons with Starbursting Galaxies

Figure 3.3 shows a comparison plot between SHARK and the observational results from [Lo Faro et al. \(2015\)](#). A comparison with [Sargent et al. \(2010b\)](#) is also made. This figure shows is a test of the SHARK model in the extreme regime of (U)LIRGs. Error bars for all properties from [Lo Faro et al. \(2015\)](#) is the median error of each of the populations; no individual errors were provided for any property.

[Lo Faro et al. \(2015\)](#) uses a sample first published in [Fadda et al. \(2010\)](#) and is an extension to the analysis done in [Lo Faro et al. \(2013\)](#) using the Spitzer Space Telescope to find the MIR spectroscopy and Hershel Space Observatory for FIR photometry and the VLA at 1.4GHz for radio data. The sample from [Fadda et al. \(2010\)](#) was designed to characterise the properties of sources which contribute to the Cosmic Infrared Background (CIB). It has been shown that the main contributors to the CIB are sub mJy sources at $24 \mu\text{m}$ with a main peak at $z \sim 1$ and a secondary peak at $z \sim 2$ ([Lagache et al. 2005](#)). At these redshifts, sub-mJy IR sources would be LIRGs at $z \sim 1$ and ULIRGs at $z \sim 2$, which is the definition that [Fadda et al. \(2010\)](#) uses in classifying the galaxies.

In the observational data used here, LIRGs are classified as having $S(24\mu\text{m})$ $0.2 - 0.5$ mJy at $z = 0.76 - 1.05$. ULIRGs are classified as having $S(24\mu\text{m})$ $0.14 - 0.55$ mJy at $z = 1.75 - 2.4$.

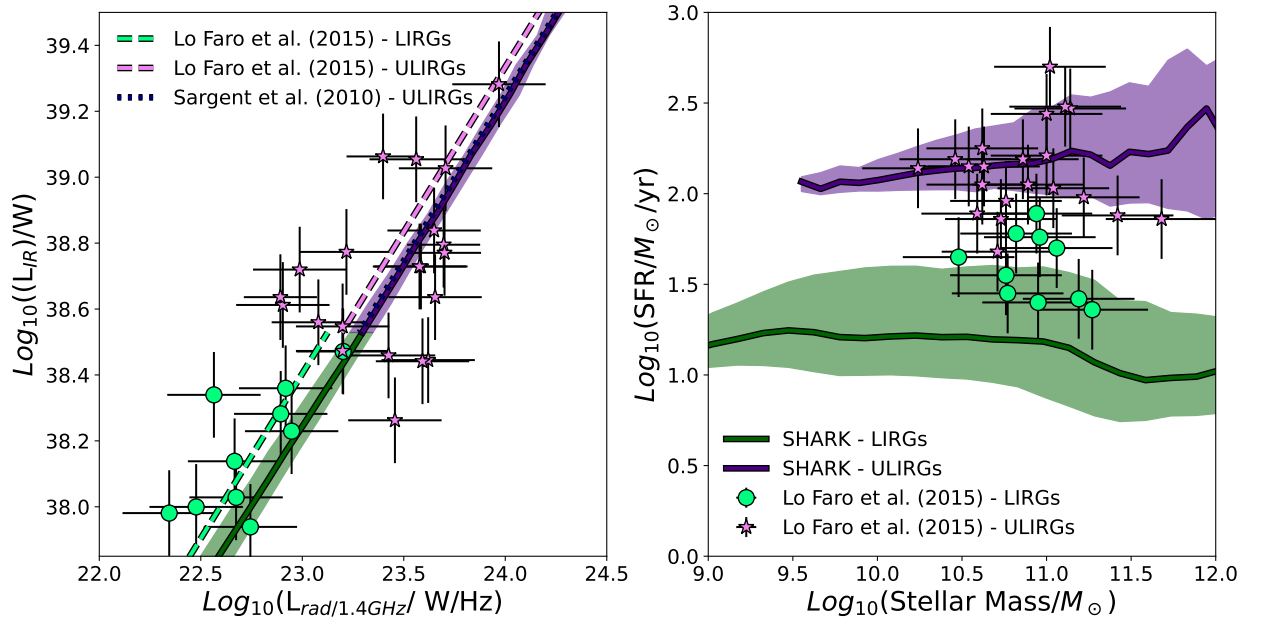


Figure 3.3: Comparison plots with observational data of individual (U)LIRGs from Lo Faro et al. (2015). The circles are the observational data from Lo Faro et al. (2015) of LIRGs and stars are ULIRGs. The blue area is LIRGs and the red area is ULIRGs from the SHARK with radio luminosity calculated using our model. The right plot shows L_{IR} vs. $L_{rad}(1.4GHz)$ and the left plot shows SFR vs. total stellar mass. LIRGs from SHARK have been selected as having a total $10^{11} L_{\odot} < L_{IR} < 10^{12} L_{\odot}$ and ULIRGs have been selected as having a total $10^{12} L_{\odot} > L_{IR}$. These are the same parameters that constrain the (U)LIRGs found in Lo Faro et al. (2015). No selection with redshift have been made of the SHARK galaxies.

This differs from the usual definition of LIRGs having IR luminosity $10^{11} - 10^{12}L_{\odot}$ and ULIRGs having IR luminosity of $10^{12} - 10^{13}L_{\odot}$, which is the definition I use in SHARK. It also rules out any Hyper Luminous InfraRed Galaxies (HyLIRGs) and Extremely Luminous Infrared Galaxies (ELIRGs) which are usually defined as having an IR luminosity of $10^{13} - 10^{14}L_{\odot}$ (Cutri et al. 1994) and $> 10^{14}L_{\odot}$ (Tsai et al. 2015) respectively, however no galaxies in this sample has an IR luminosity $> 10^{13}L_{\odot}$.

The stellar mass of the galaxies are determined using SED fits using two different codes: Fadda et al. (2010) and Lo Faro et al. (2013) use HYPERZ (Bolzonella et al. (2000) while Lo Faro et al. (2013) and Lo Faro et al. (2015) uses GRASIL (Silva et al. 1998). (Further, more specific details of how these fits are completed are present in the three separate papers). The stellar mass shown here is that which has been found using HYPERZ. The reason for this is because in modelling the radio frequencies of the SEDs, GRASIL invokes the Bressan model; the same model that is used here to model radio emission (Vega et al. (2005)). While Lo Faro et al. (2013) does use GRASIL to find the stellar mass using FIR photometry and MIR spectroscopy and hence would not invoke the Bressan model in using GRASIL, to avoid any potential circularity, I use the results from HYPERZ. Lo Faro et al. (2013) finds that the GRASIL finds higher stellar mass than HYPERZ, Figure 3.3 shows that the stellar mass ranges are in broad agreement with that found in SHARK (The differences in the GRASIL and HYPERZ stellar masses are not that significant on these scales in any case).

GRASIL is also used derive the SFR in Lo Faro et al. (2013) and Lo Faro et al. (2015), however the SFR is also calculated using the SFR- L_{IR} relation from Kennicutt Jr (1998). This relation is shown in Equation 3.1.

$$SFR = \frac{L_{FIR}}{5.8 \times 10^9 L_{\odot}} \quad (3.1)$$

Equation 3.1 was calculated for a Salpeter IMF (Salpeter 1955), however this was rescaled to a Chabrier IMF in Lo Faro et al. (2013). For the same reasons discussed above, I adopt the SFR found using Equation 3.1.

One of the results of Lo Faro et al. (2013) was to show that, at least for (U)LIRGs, that the Kennicutt Jr (1998) produces a SFR 1.7 - 2.5 higher than the result from GRASIL. This is because the Kennicutt Jr (1998) method include significant "cirrus" emission from intermediate-age stellar populations which contribute to dust heating. Figure 3.3 shows that SHARK produces SFR that are lower than that calculated using the relation from Kennicutt Jr (1998) for LIRGs, but, on average, produce SFRs that are comparable for ULIRGs.

Lo Faro et al. (2015) also use GRASIL to fit for L_{IR} and $L_{1.4\text{GHz}}$, but present that which is calculated directly from observations. I use here the results direct from observations, without invoking GRASIL.

As an aside, Lo Faro et al. (2015) finds excellent agreement with the $L_{1.4\text{GHz}}$ as derived from GRASIL and the observations. From this it is not surprising that SHARK finds broad agreement with these observations using the same model.

3. RESULTS

AGNs are identified in [Fadda et al. \(2010\)](#) and excluded in [Lo Faro et al. \(2013\)](#) using several different AGN indicators including: (i) broad and high ionisation lines for those galaxies with optical spectra, (ii) SED fitting, (iii) X-Ray brightness (for sources with X-Ray observations), (iv) strength of $6.2 \mu\text{m}$ Polycyclic Aromatic Hydrocarbons (PAH) features and (v) optical morphology. The overall sample is crudely luminosity selected and results in 31 (U)LIRGs in the sample.

[Sargent et al. \(2010b\)](#) studied ULIRGs out to $z < 2$ using the VLA-COSMOS "Joint" Catalogue. This is an IR selected sample and they found that $q_{\text{IR}} = 2.672^{+0.121}_{-0.121}$ that is independent of redshift. This includes 1692 star-forming ULIRGs and 3004 'IR bright' sources. AGNs are removed from this sample using a method derived in [Smolčić et al. \(2008\)](#). Briefly, this method uses the rest frame $(u - K)$ colours and relies on the correlation between these colours and the BPT diagram.

The SHARK population of galaxies are chosen to following the definitions of (U)LIRGs given in [Fadda et al. \(2010\)](#): LIRGs having L_{IR} between $10^{11} - 10^{12} L_{\odot}$ and ULIRGs have $L_{\text{IR}} > 10^{12} L_{\odot}$. Note that unlike [Lo Faro et al. \(2015\)](#), no redshift selection has been taken for (U)LIRGs. Including a redshift selection did not drastically change the results shown in Figure 3.3 and so a broader population of galaxies was chosen in order to compare with here.

The left panel of Figure 3.3 shows the L_{IR} to $L_{1.4\text{GHz}}$ relation and hence the existence of the FIRC in (U)LIRGs. It shows that the medians from [Lo Faro et al. \(2015\)](#) does not necessarily agree well with SHARK, but the results from [Sargent et al. \(2010b\)](#) agrees very well with SHARK (So much that it is hard to see!)

The reason for this discrepancy between [Lo Faro et al. \(2015\)](#) and [Sargent et al. \(2010b\)](#) is sample size. [Lo Faro et al. \(2015\)](#) only has a total sample size of 31 galaxies whereas [Sargent et al. \(2010b\)](#) has a sample size of over 3000. This is a dramatically more robust and statistically significant sample. Hence, it is not concerning that the median of [Lo Faro et al. \(2015\)](#) does not agree with SHARK and heartening that the median of [Sargent et al. \(2010b\)](#) does. That being said, [Sargent et al. \(2010b\)](#) does not offer any other characteristic measurements, like stellar mass or SFR, whereas [Lo Faro et al. \(2015\)](#) does.

It is important to remember that the results from SHARK show the median and uncertainty of an entire population, whereas the points from [Lo Faro et al. \(2015\)](#) shows the results of individual galaxies. Thus, that there are individual points away from the SHARK median is to be expected. In any case, nearly all of the points are within their margin of error of the median from SHARK.

Another reason why the median of [Lo Faro et al. \(2015\)](#) is higher than that of SHARK is selection biases within the observational sample. The [Fadda et al. \(2010\)](#) only selected galaxies with available optical and near IR data with which properties could be derived. As these galaxies are at high redshift, they would require a high optical luminosity. Such galaxies might be biased towards higher IR and radio luminosities, even within the (U)LIRG regime. This would lead to a q_{IR} that is the same slope, but shifted across towards higher L_{IR} .

The main takeaway from the left figure is that the FIRC exists in (U)LIRGs within SHARK, in

line with the observations from [Sargent et al. \(2010b\)](#) and [Lo Faro et al. \(2015\)](#).

The right panel of Figure 3.3 shows the SFR-stellar mass relation. This shows that for SHARK, (U)LIRGs do not evolve significantly over the SFR-stellar mass relation (though no evolution was expected). It also shows that (U)LIRGs in SHARK produce a high SFR despite no SFR selection was made in the population.

This shows excellent agreement between SHARK and [Lo Faro et al. \(2015\)](#) in terms of ULIRGs, but less agreement in terms of LIRGs. This disagreement is not fatal; I am comparing individual galaxies to a population after all so some scatter is expected. Further, most of the LIRGs are within the $1 - \sigma$ range of the SHARK population, but it is worth discussing all the same

This could be due to [Kennicutt Jr \(1998\)](#) systemically producing higher SFR, as [Lo Faro et al. \(2013\)](#) found. This would increase the SFR of each of the LIRGs beyond normal leading to the disagreement that is seen here. That ULIRGs do agree with SHARK is also because of this systemically high SFR and that the definitions used to classify (U)LIRGs used here are different. There are some ULIRGs with IR luminosity $< 10^{11} L_{\odot}$ in the observational sample. These galaxies are excluded by definition in the SHARK ULIRGs. Hence, compared with the SHARK ULIRGs, the observational ULIRGs will have a lower IR luminosity. In estimating the SFR as proportional to IR luminosity, this lower IR luminosity would produce a lower SFR. This affect appears to cancel out the systemic over estimation of SFR that the [Kennicutt Jr \(1998\)](#) method has.

It is also indicative of a sample that is biased towards high IR galaxies. If the sample does contain uncharacteristically high IR, then this would produce a high SFR by definition when using a $L_{IR} - SFR$ relation.

Further, [Fadda et al. \(2010\)](#) showed that the sample was biased towards galaxies that contain PAH features. PAHs trace cold molecular gas where star formation is optimal and hence are understood to trace star formation ([Li 2020](#)). This means this is a sample of galaxies that have a high IR emission and PAH features, meaning they are doubly biased towards galaxies with high SFRs. This bias could cause the increase in LIRGs seen here.

While there are differences between the observations from [Lo Faro et al. \(2015\)](#) and Shark they are really academic. The median SHARK result is within the margin of error for most of the observations. The overall point of this figure is that even in the extreme (U)LIRG regime, the SHARK model reproduces what is seen observationally. I can therefore have confidence that this model, on average, produces physically meaningful results.

Radio Luminosity Functions at $z \geq 0$

Like the left panel of Figure 3.2, Figure 3.4 shows the radio LF at 1.4GHz compared with observations from [Bonato et al. \(2021a\)](#), [Butler et al. \(2019\)](#), [Novak et al. \(2017\)](#) and [Ocran et al. \(2019\)](#) except over multiple redshifts. The same method as outlined in section ?? was followed here. As in Figure 3.2, the blue line shows the radio LF with no convolution and the red line shows the radio LF convolved with a Gaussian with mean = 0 and a standard deviation = 0.3.

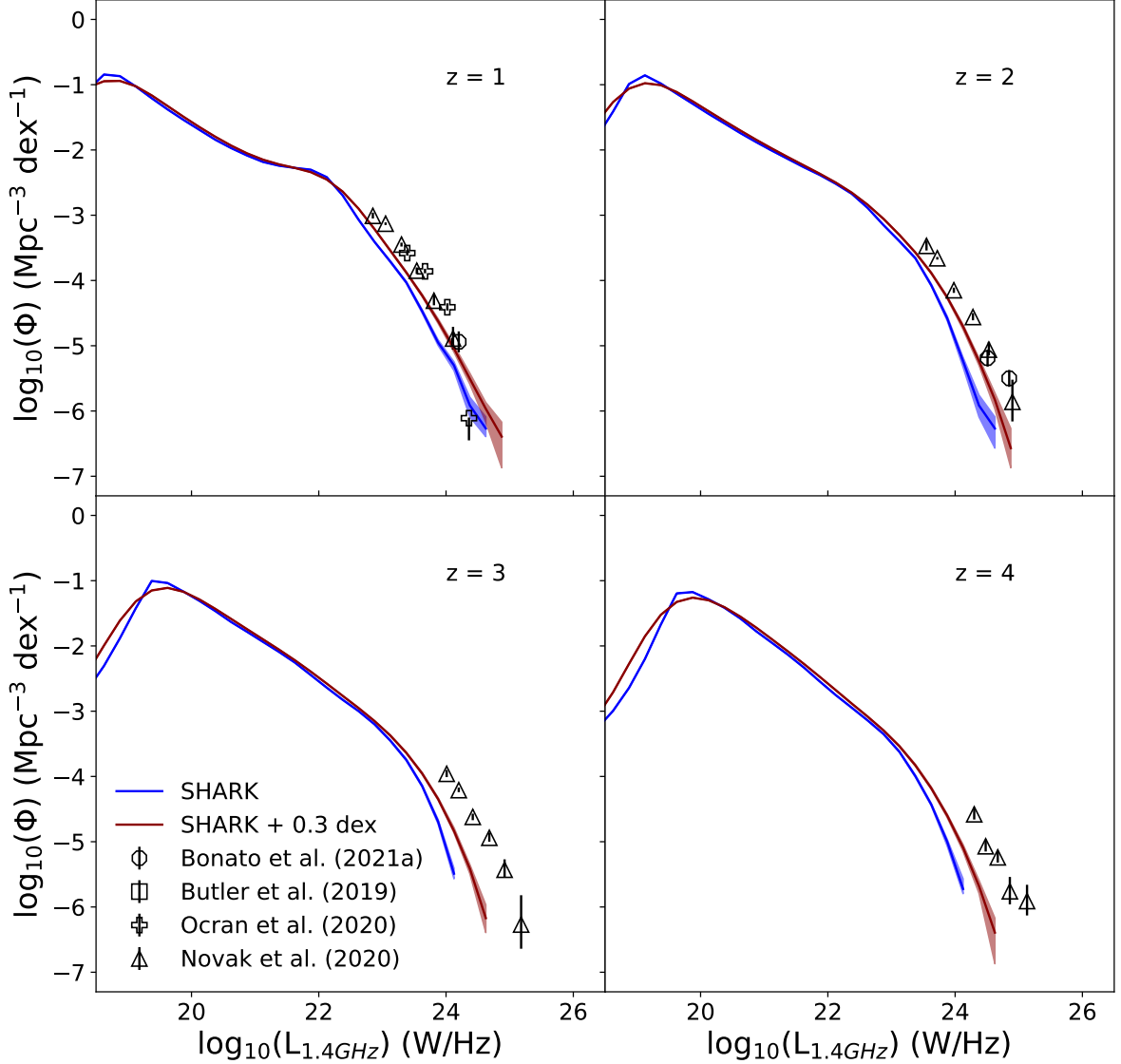


Figure 3.4: The radio LF for all galaxies for different redshifts for frequency of 1.4GHz. Top-left panel shows $z = 1$, top right panel shows $z = 2$, bottom left panel shows $z = 3$ and bottom right panel shows $z = 4$. Much of the details here are the same as in Fig. 3.2; the blue line shows the median with no convolution and the orange shows the same but convolved with a Gaussian with mean = 0 and 0.3 standard deviation. Comparisons are made with observational data of SFGs from Bonato et al. (2021a), Butler et al. (2019), Novak et al. (2017) and Ocran et al. (2019). The shaded region shows the $1 - \sigma$ area estimated using bootstrapping.

The shaded region shows the $1 - \sigma$ error estimated using bootstrapping.

Figure 3.4 shows that there is less agreement between the SHARK model radio LF with observations at higher redshifts. At $z = 1$, the observational data agrees more with the convolved line than the non-convolved line. This is true at $z = 2$ as well. The purpose of this convolved line is to estimate the errors present in these observations like cosmic variance, low sample sizes and AGN contamination which have not been accounted for in the observational data. That the observational data agrees more with the convolved line shows that the regular SHARK model is under predicting the radio LF compared with observations.

At $z = 3$ and $z = 4$, neither the convolved line nor non-convolved line agrees with the observational data from [Novak et al. \(2017\)](#). At these redshifts, the SHARK model under predicts the radio LF compared with observations, but to a much greater degree than at $z = 1$ and $z = 2$.

There are similar trends present in Figure 3.5. Here the radio LF is shown for 150MHz for redshifts 1, 2, 3 and 4. This is compared with observational results from [Bonato et al. \(2021b\)](#). Note that the results from [Bonato et al. \(2021b\)](#) has been binned into larger redshift bins (ie $0.8 < z < 1.0$ and $1.0 < z < 1.2$) so where applicable, I show two sets of bins that cover the redshift under consideration.

As in Figure 3.4, at $z = 1$ and $z = 2$, the observational data agrees more with the convolved SHARK model than the non-convolved model. Whereas at $z = 3$ and $z = 4$, neither the convolved model nor non-convolved model agrees with observations.

Here I will discuss three possibilities for this discrepancy: that SHARK requires a top-heavy IMF, that SHARK underpredicts the SFR and that the observations include AGN contamination.

As discussed in section 3.0.1, previous studies into modelling the UV and IR LF have had similar problems in that the models were under predicting the LF compared with observational results. Invoking a top heavy IMF within such models appears to rectify the issue in these studies ([Baugh et al. 2005](#); [Lacey et al. 2008](#); [Camps et al. 2016](#); [Cowley et al. 2019](#); [Trčka et al. 2020](#)). I argue that this is not the case in SHARK. SHARK uses the [Chabrier \(2003\)](#) IMF, which is not top heavy, yet Figure 3.2 shows excellent agreement with observations at $z = 0$. Further [Lagos et al. \(2019\)](#) showed that the UV - IR LFs can be reproduced in SHARK using the same [Chabrier \(2003\)](#) IMF. It would require an uncomfortable level of fine tuning to require a top-heavy IMF for $z > 0$ but not $z = 0$.

Another possibility which is discussed in the literature is that the SFR in the model is too low ([Somerville et al., 2012](#)). This issue is particularly pertinent in SHARK as the radio emission is modelled proportional to the SFR (See the Methods section). This possibility is tested in Figure 3.6.

Figure 3.6 shows the SFR function as derived in SHARK. The method of determining the SFR function in SHARK follows closely the process used in determining in the radio LFs. At each redshift, a histogram with equal bin sizes is created from the SFR of all galaxies present. At this point, the histogram undergoes bootstrapping to determine the $1 - \sigma$ uncertainty. The histogram and errors are then divided by the total volume of the simulation (for all 64 snapshots this is $210\text{Mpc}^3 \times 64$ snapshots) and the bin width.

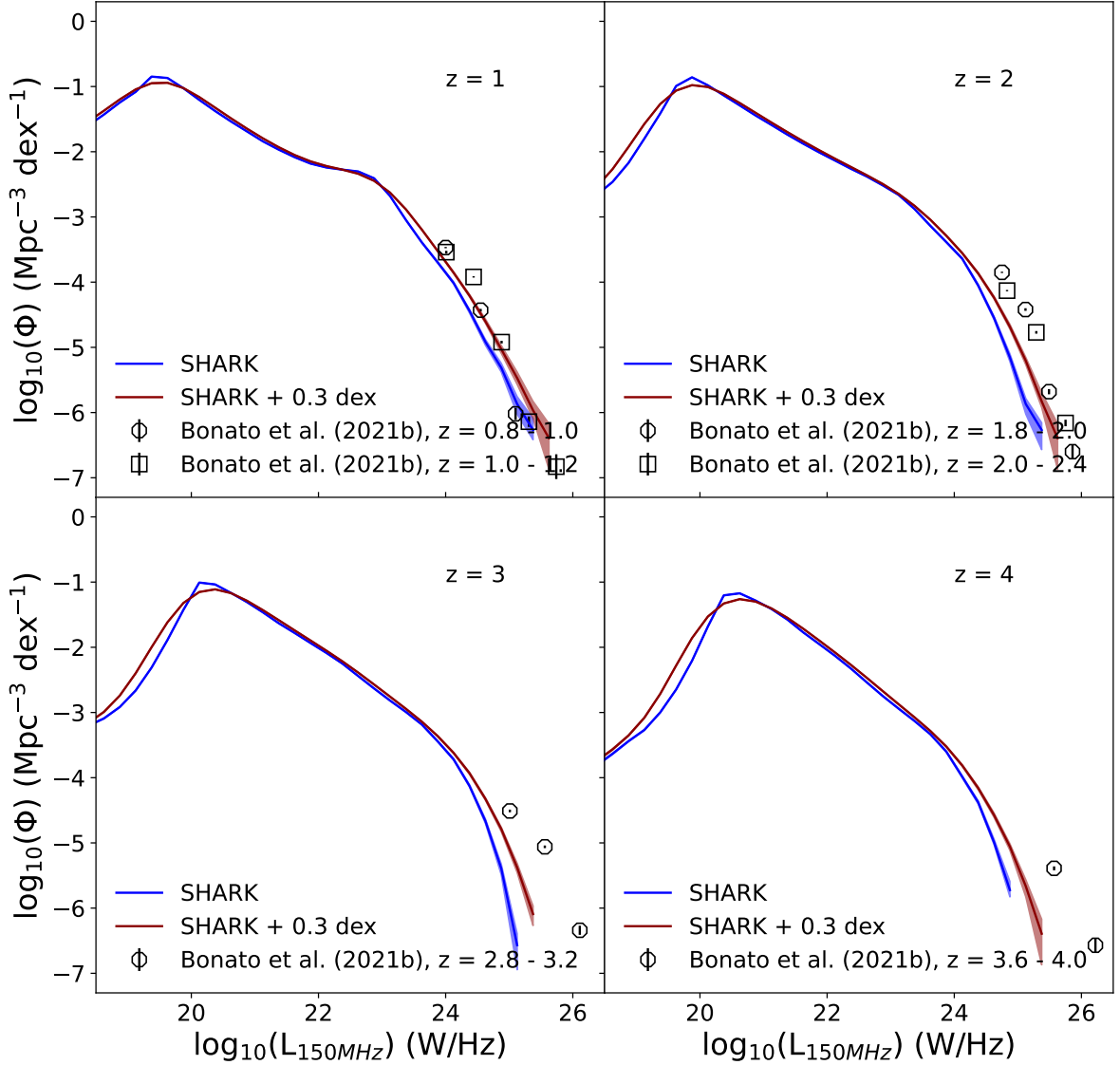


Figure 3.5: The radio LF for all galaxies for different redshifts for frequency of 150MHz. As in Fig. ??, top-left panel shows $z = 1$, top right panel shows $z = 2$, bottom left panel shows $z = 3$ and bottom right panel shows $z = 4$. Much of the details here are the same as in the right hand panel of Fig. 3.2; the blue line shows the median with no convolution and the orange shows the same but convolved with a Gaussian with mean = 0 and 0.3 standard deviation. Comparisons are made with observational data of SFGs from Bonato et al. (2021b). The shaded region shows the $1 - \sigma$ area estimated using bootstrapping.

This is compared with observational results from [Katsianis et al. \(2017\)](#). This paper focuses on the evolution of the SFR function in the EAGLE simulation, but to do so derives the SFR function from observations. [Marchetti et al. \(2016\)](#), [Mauch & Sadler \(2007\)](#), [Patel et al. \(2013\)](#), [Robotham et al. \(2011\)](#), [Alavi et al. \(2016\)](#) and [Bouwens et al. \(2015\)](#) (among others used in [Katsianis et al. \(2017\)](#)) derive LFs for their respective tracers (IR, UV, radio etc.). These LFs are then converted to SFRs using relations derived for those tracers. More details of the methods used is present in [Katsianis et al. \(2017\)](#).

What Figure 3.6 shows is that SHARK agrees with the SFR derived from observations across different redshifts and different tracer methods. This agreement is in contrast to previous galaxy emission models which under predicted the SFR ([Somerville et al., 2012](#)). This therefore refutes the idea that the tensions between SHARK and observed radio LFs is due to an underprediction of the SFR.

The third possibility I will discuss for the discrepancy between the SHARK and observed radio LFs is that observations contain AGN contamination of what should only contain SFGs. The removal of AGNs is treated differently in each paper (See section 3.0.1 for details). For example, [Novak et al. \(2017\)](#) determines AGN dominated galaxies using a three component SED fit. They also remove radio excess sources by determining the IR derived SFR and construct histograms of $\log_{10}(\text{SFR}/\text{radio})$. By the FIRC, the SFR derived from IR and the radio luminosity should be well correlated. Thus they define radio excess sources as being 3σ above the median of these histograms.

Such a method is fine for identifying radio loud AGNs, but as [Novak et al. \(2017\)](#) notes: "We are...not interested in removing all AGN host galaxies from our sample, but only those that show clear evidence of radio emission dominated by an AGN." Hence, AGN contamination is present in these radio LFs. AGN contamination would arbitrarily increase the radio luminosity of each point, which would explain SHARK's apparent under prediction in Figure 3.4.

But if AGN contamination is the reason for the tension in Figures 3.4 and 3.5, then why is this not present at $z = 0$? This comes down to the ease for which AGNs can be identified at low redshifts compared with high redshifts. For example the BPT diagram used to identify AGNs in the GAMA data is unusable at $z > 0.4$. This is because emission lines required to construct a BPT diagram are shifted into the IR spectrum where deriving spectra becomes increasingly difficult ([Trouille et al. \(2011\)](#)). To that end there is a difficulty in attaining a clean sample of SFGs at high redshifts that is free of AGN contamination.

3.0.3 The Far-Infrared Radio Correlation

In this section, I turn to the FIRC and how SHARK can model the its relationships with other parameters. A benefit of any galaxy simulation is that a wide array of galaxy properties is tracked across the population. This makes SHARK an ideal testing ground for FIRC and our understanding of the physics behind it. Previous Figures have shown that SHARK reproduces FIRC for SFGs (Figure 3.1) and (U)LIRGs (Figure 3.3). In this section I discuss the FIRC in

3. RESULTS

terms of q_{IR} as defined in Equation ??.

3.0.4 Evolution of q_{IR} with M_*

In a recent paper, [Delvecchio et al. \(2021\)](#) found that rather than redshift, q_{IR} evolves with M_* . I begin my analysis of q_{IR} by examining whether this is true in SHARK as well.

Figure 3.7 shows the evolution of q_{IR} with M_* with the number counts of galaxies. All galaxies from SHARK with $10^8 M_\odot \leq M_* \leq 10^{12} M_\odot$ and $0 \leq q_{\text{IR}} \leq 3.3$ at $z = 0$. Only cells with more than 100 galaxies are displayed. The median line and $-\sigma$ lines are of the same population, but are also influenced by M_* bins with fewer than 100 galaxies (This is why the median line appears to extend beyond the coloured region).

There do exist galaxies outside of this range however I do not display them here. Too few galaxies above $10^{12} M_\odot$ are present to be plotted (This is evident by the number of blank cells above $11.5 M_\odot$). Galaxies below $10^8 M_\odot$ do not necessarily have physical counterparts. Galaxies with $q_{\text{IR}} > 3.3$ do exist, but again are too few to be plotted meaningfully here. There are a substantial amount of galaxies with $q_{\text{IR}} < 0$, but they had unphysical SFRs (on the order of $10^{-5} M_\odot \text{yr}^{-1}$), so have been excluded accordingly. In any case, plotting with the entire q_{IR} range gives a similar median line seen here, so including or excluding these galaxies would not make a substantive difference.

For $M_* \geq 10^{10} M_\odot$ has only a single population centered around $q_{\text{IR}} \sim 2.7$. This is on the scale that agrees with most observational results of q_{IR} (ie [Bell \(2003\)](#) found $q_{\text{IR}} = 2.64 \pm 0.02$). It is evident that this population extends to $M_* \leq 10^{10} M_\odot$ as well, but the median descends to as low as $q_{\text{IR}} \sim 1.5$ at $M_* \sim 10^{8.5}$. This is due to the influence of a second population that has a lower q_{IR} . This second population has a q_{IR} as low as ~ 0.0 , but increases with a constant slope to meet the original population at $M_* \sim 10^{9.5} M_\odot$. The lower q_{IR} population is something of an anomaly; as best I can tell such divergent populations have not been observed or predicted in previous works.

With this as the starting point, the forthcoming plots will investigate the physical properties of this population of galaxies and explain why it exists.

Is it Infrared or Radio that causes this dip in q_{IR} ?

By Equation ?? a decrease in q_{IR} as seen in Figure 3.7 can either be caused by a decrease in L_{IR} or an increase in L_{radio} . Figure 3.8 shows that this is because of a decrease in L_{IR} .

Figure 3.8 shows q_{IR} against M_* coloured by median IR luminosities (left column) and median radio luminosities (right column) properties. These plots focus in on masses $8_\odot \leq \log_{10}(M_*) \leq 9$ since these are the masses where the divergence is strongest. The top row shows IR and radio luminosities, with no normalisation in W and W respectively. Broadly this shows the expected behaviour of increasing luminosity with M_* . It is also clear that the lower q_{IR} population has a lower L_{IR} at the same M_* . L_{rad} would have to increase in order to produce the same effect on q_{IR} and it is not increasing. However, for completeness, I include the second rows for a

For that reason I normalise the luminosities to M_* in the second row. To do this, I divide the luminosities of each galaxy by its M_* , so that any evolution due to M_* is factored out. A clear picture forms for L_{IR} in this plot: for the higher, more constant q_{IR} , L_{IR}/M_* is constant and on the high end of the plot. However for the lower, but increasing population of q_{IR} , L_{IR}/M_* increases with increasing q_{IR} .

The normalised L_{rad} plot, on the other hand, is similar, but not quite as clear. The higher, constant population does have a high normalised L_{rad}/M_* and the lower, increasing q_{IR} population see a similar increase in L_{rad}/M_* to that seen in the L_{IR}/M_* , but it is not as clear cut. These trends are general and there is a significant amount of scatter in these results. Further, the different scales used in L_{IR} and L_{rad} mean that a one-to-one comparison is not useful. The extent to which the luminosities change may be exaggerated if the limits of the colour scale are too small.

It is for that reason that in the final row of Figure 3.8, I plot ΔL_{IR} and ΔL_{rad} . ΔL_{IR} is defined as the distance from the median of the L_{IR}/M_* . The full definition is given in Equation 3.2:

$$\Delta L_{IR} = L_{IR}/M_*/[W/M_\odot] - median(L_{IR}/M_*/[W/M_\odot]) \quad (3.2)$$

This puts the differences in L_{IR} and L_{rad} on the same scale. The colour scale in the final row is deliberately set to $[-1, 1]$ to highlight the amount of difference between the two luminosities. What this confirms is the significance that L_{IR} has on q_{IR} . The ΔL_{IR} extends over the entire $[-1, 1]$ range and increases with increasing q_{IR} . ΔL_{rad} , on the other hand, does increase with increasing q_{IR} , but its change does not extend over the entire range, instead a limited portion of it.

While the decreasing L_{rad} is not as impactful on q_{IR} than the decreasing L_{IR} (for the simple reason that L_{IR} decreases more), it is still important to note. The decreasing L_{rad} complicates the analysis as individual processes may influence L_{rad} or L_{IR} or perhaps both.

Overall, what can be concluded from this plot is that the decreasing q_{IR} is defined by a lower than average L_{IR} . In the next section, I will examine some of the properties of these galaxies to try and elucidate the physical characteristics of these lower q_{IR} galaxies.

The Physical Characteristics of lower q_{IR} galaxies.

Figure 3.9 shows the same population of SHARK galaxies as in Figure 3.8, but coloured by different properties. These properties have been chosen because they either clearly indicate some diverging properties between the two q_{IR} populations or in previous papers a correlation between the property and q_{IR} has been found (or in the case of T_{eff} , both).

The upper left plot is coloured by effective dust temperature (T_{eff}). In SHARK, T_{eff} is not calculated directly, instead it is approximated using Equation 3.3

$$T_{eff} = T_{BC} \times L_{IR,BC} + T_{diff} \times (1 - L_{IR,BC}) \quad (3.3)$$

3. RESULTS

Where $T_{BC} = 50K$ is the temperature of the birth clouds, $T_{diff} = 25K$ is the temperature of the diffuse ISM and $L_{IR,BC}$ is the total IR emission from birth clouds as calculated from the formalism in [Lagos et al. \(2019\)](#). The temperatures of the birth clouds and diffuse dust have been set somewhat arbitrarily and so this is only an approximation. Modelled in this way T_{eff} acts as a measure of the strength of the contribution from birth clouds on the IR spectrum.

The T_{eff} plot then shows that high, constant q_{IR} is cooler and lower, increasing q_{IR} population is much hotter. Hence, the population of high, constant q_{IR} is dominated by emission from the cold ISM, whereas the emission from the lower, increasing q_{IR} is dominated by emission from hot birth clouds.

[Smith et al. \(2014\)](#) and [Ivison et al. \(2010a\)](#) also found a similar negative correlation between T_{eff} and q_{IR} . In particular, [Smith et al. \(2014\)](#) found that this relationship strengthens at longer IR wavelengths. The explanation that was given is since blackbody radiation has a strong dependence on wavelength, the smaller, hotter birth clouds can overcome the larger, cooler ISM. But these hot wavelengths are shorter than at hotter temperatures so will fade faster than the longer, cooler wavelengths.

SHARK agrees with this finding. When a galaxy's IR emission is dominated by hot birth clouds, the integrated IR emission will have a greater contribution from shorter wavelengths. However, since these wavelengths fade faster than longer wavelengths, the total IR emission is reduced. This in turn reduces the IR as seen in Figure 3.8 and the overall reduction in q_{IR} seen in this section.

As M_* increases though, the proportion of birth clouds to disks shrinks. The birth clouds struggle to dominate over the increasingly massive ISM, which starts to contribute a greater proportion of the IR emission. This is why as M_* increases, the lower q_{IR} also increases until the emission from the ISM completely dominates the emission from birth clouds.

This explains the reason why the T_{eff} looks as it does.

The upper right plot is coloured by the normalised total gas mass (M_{gas}). This is defined as by Equation 3.4:

$$M_{gas} = \frac{M_{gas,bulge} + M_{gas,disk}}{M_*} \quad (3.4)$$

where $M_{gas,bulge}$ and $M_{gas,disk}$ is the mass of the gas in the bulge and disk respectively, both in M_\odot .

Total gas mass has a strong dependence on M_* , so to remove any contribution from this evolution and instead focus on any evolution with q_{IR} , I have chosen to normalise it against M_* .

Both $M_{gas,bulge}$ and $M_{gas,disk}$ are fundamental baryonic quantities that SHARK models directly. They are both tracked for galaxy and are easily accessible at the end of each snapshot (See Equations 49-64 in [Lagos et al. \(2018\)](#)). Both $M_{gas,bulge}$ and $M_{gas,disk}$ includes atomic gas and gas locked up in metals.

The M_{gas} figure in Figure 3.9 shows a complex picture. As it appears, particularly at $M_* \sim 10^8 - 10^{8.4}$, a higher q_{IR} can imply a higher M_{gas} . As best I can tell, there are no other studies

that have compared q_{IR} with M_{gas} , so the analysis here is purely based on SHARK.

However, I contend that this matches the same picture as seen with T_{eff} . Within the same M_* bins, a higher M_{gas} means that the gas to M_* ratio is higher. Hence, the ISM to birth cloud ratio is also higher. Thus, emission from the ISM will more easily dominate over the IR emission, making it more regulated.

The middle left plot is coloured by the half-mass radius of the disk ($r_{0.5\text{mass}}$). This is an indicator of the total size of the galaxy. Like $M_{\text{gas,bulge}}$ and $M_{\text{gas,disk}}$, $r_{0.5\text{mass}}$ is directly tracked in SHARK, so it is simple to access them at the end of each snapshot.

What this shows is that within the same M_* bin, higher q_{IR} will have a smaller $r_{0.5\text{mass}}$ meaning that they are smaller than galaxies with lower q_{IR} . Like M_{gas} this is tracked directly in SHARK, so is easily accessed at the end of each snapshot.

Being bigger in size at the same M_* makes a galaxy more dispersed.

The middle right panel is coloured by gas surface density (Σ_{gas}). The gas surface density is found via Equation 3.5.

$$\Sigma_{\text{gas}} = \frac{M_{\text{gas}}}{2\pi r_{0.5\text{mass}}^2} \left[\frac{M_{\odot}}{\text{Mpc}^2} \right] \quad (3.5)$$

What this panel shows is evolution of q_{IR} with Σ_{gas} . Lower Σ_{gas} is associated with lower q_{IR} .

The lower left plot is coloured by specific star-formation rate (sSFR). sSFR is defined in the usually way being SFR/M_* . As SHARK models L_{sync} as directly proportional to SFR and at 1.4GHz synchrotron radiation dominates over free-free emission, this makes SFR an indicator of radio emission. SFR is known to evolve with M_* however, so sSFR is used here to reduce the effect of this evolution.

What the sSFR plot shows is a negative correlation between sSFR and q_{IR} . This gives some explanation as to the decreasing L_{rad} seen in Figure 3.8. A decreasing sSFR means that there are less CCSNe to accelerate CRs to synchrotron wavelengths.

The lower right plot is coloured by SFR surface density (Σ_{SFR}). Σ_{SFR} is defined in a similar way to Σ_{gas} :

$$\Sigma_{\text{gSFR}} = \frac{\text{SFR}}{2\pi r_{0.5\text{mass}}^2} \left[\frac{M_{\odot}}{\text{yr Mpc}^2} \right] \quad (3.6)$$

This shows a weak correlation between Σ_{SFR} and q_{IR} , particularly at low M_* . Though it is important to note the strong correlation shown between Σ_{SFR} and M_* that appears to over-power this relation.

This is different to what was found in [Delvecchio et al. \(2021\)](#), which found an anti-correlation between q_{IR} and Σ_{SFR} . Seemingly driven by SFR, they see this relation independent of M_* . It is also in contrast to the models in [Lacki et al. \(2010\)](#), which predicted a anti-correlation as well, but steeper than what was found in [Delvecchio et al. \(2021\)](#).

This result is a combination of the result of sSFR and half-mass radius. Those plots showed an increased half-mass radius and an increase sSFR. It appears that there might be a conspiracy

3. RESULTS

whereby these two seem to cancel each other out when combined into Σ_{SFR} .

Taken together, the individual plots of Figure 3.9 show that those galaxies with lower L_{IR} in SHARK have: (i) high T_{eff} and are thereby dominated by birth cloud emission, (ii) less gas, (iii) are larger and more disperse, (iv) lower Σ_{gas} , (v) lower sSFR and (vi) lower Σ_{SFR} . These properties will be brought together in Section 4 where I bring together the consequences of these results on our understanding of galaxy formation.

Figure 3.10 shows the IRX- β plane for SHARK galaxies coloured by their q_{IR} value. Only cells with more than 100 galaxies within are shown.

The IRX- β relation is used as a measure of dust attenuation (Reddy et al. 2018). It is widely thought that the UV radiation emitted by young, massive stars is absorbed by the surrounding dust and re-emitted as IR radiation. The amount of excess IR (IRX) (as defined in Equation ??) represents how much UV radiation is absorbed and re-emitted in this process. A high IRX means more UV absorption and hence a high UV optical depth and a lower IRX means less UV absorption and a lower UV optical depth

$$\text{IRX} = \frac{L_{\text{IR}}}{L_{\text{UV}}} \quad (3.7)$$

β is the UV spectral slope and is a measure of how the intensity of light changes with λ .

$$f_{\lambda} \propto \lambda^{\beta} \quad (3.8)$$

where f_{λ} is the observed flux (Calzetti et al. 1994). β is often used as a proxy for the amount of dust obscuration (Reddy et al. 2018).

As discussed in the method section, Lagos et al. (2019) provides the UV-IR SED for all SHARK galaxies. The luminosities required here are found easily from these results. The L_{IR} is the total luminosity integrated over $8 - 100\mu\text{m}$ (As it is through out this paper). L_{UV} used in the IRX calculation is at 1500\AA . To calculate the β of each galaxy, the L_{UV} at 1500\AA and 2500\AA is calculated. The ratio of these fluxes and the wavelengths used readily gives β for each SHARK galaxy.

The galaxies shown in the hexbin of 3.10 is a subset of all galaxies from SHARK. The parameters for selecting this subset is; (i) all galaxies with a gas metallicity ($Z_{\text{gas}} > 0$) (Z_{gas} calculated following Equation 3.9) are included.

$$Z_{\text{gas}} = \frac{(M_{Z,\text{disk}} + M_{Z,\text{bulge}})}{(M_{\text{gas,disk}} + M_{\text{gas,bulge}})} \quad (3.9)$$

Where $M_{Z,\text{disk}}$ and $M_{Z,\text{bulge}}$ are the mass of metals in the disk and the bulge respectively. Both properties are tracked by SHARK from snapshot-to-snapshot. That being said, there will be some galaxies that evolve without any metals in them. Such galaxies are unphysical and so are excluded.

(ii) Only central galaxies as defined in SHARK are included. The definition of a central galaxy is involves the process by which SHARK evolves galaxies. At $z = 0$, all halos and subhalos are

found using the halo finder code VELOCIRAPTOR. The biggest subhalo within each halo is defined as the central subhalo. This process is completed iteratively back through time. The central galaxy is then the galaxy that evolves within the central subhalo. Within SHARK there are also satellite and orphan galaxies, the details of which are not important to this work, but further information is available in section 4.1 of Lagos et al. (2018).

(iii) A selection of galaxies based on their absolute magnitudes (AB) is made. Galaxies with an AB with dust between $-30 \leq AB \leq -10$ are included. This selection is made to exclude very bright and very faint galaxies that might skew the sample. The AB is taken from the results of Lagos et al. (2019). It is also to simulate a model of SF galaxies.

This is compared with the IRX- β relation found in Reddy et al. (2018). Reddy et al. (2018) found the IRX- β using observations of 3,545 SF galaxies over $z = 1.5 - 2.5$. To do so they assumed a three different dust attenuation curves, one of which is from Reddy et al. (2015), which is the one I use here.

That this curve follows the overall trend of the IRX- β relation found in SHARK is more of a confirmation of the results from Lagos et al. (2019) than this work. Instead, the colours by q_{IR} is what is significant here.

Figure 3.10 shows a strong relationship between IRX and q_{IR} . One might expect this by considering equations 1.1 and 3.7, however given observational results suggest that q_{IR} is constant, it is surprising that this occurs. What this relationship suggests is that q_{IR} has a strong relationship to dust attenuation and that less dust attenuation leads to a lower q_{IR} . That is, galaxies with lower IR have less of the UV emission absorbed by dust and re-emitted into IR wavelengths.

Comparisons with the GAMA Survey

Figure 3.1 shows q_{IR} against stellar mass for SFGs. These are the same galaxies from SHARK (All SFGs at $z = 0$) and GAMA that are shown in Figure 3.1. Again, SHARK is shown in blue, with the thick blue line showing the median of the population and the shaded blue region show $1 - \sigma$ uncertainty. The black circles shows results from GAMA.

The red line shows the Equation 5 from Delvecchio et al. (2021):

$$q_{\text{IR}}(M_*, z) = (2.646 \pm 0.024) \times A^{-0.023 \pm 0.008} - B \times (0.148 \pm 0.013) \quad (3.10)$$

where $A = (1 + z)$ and $B = \log_{10} \left(\frac{M_*}{M_{\odot}} - 10 \right)$, where I have set $z = 0$. The red shaded region shows the uncertainty that comes from this equation.

Delvecchio et al. (2021) uses IR data from the Cosmic Evolution Survey (COSMOS) using de-blended far-IR/sub mm data from Jin et al. (2018). This is combined with radio data VLA-COSMOC 3GHz Large Project from Smolčić et al. (2017). For calculating q_{IR} , this 3GHz data is converted to 1.4GHz assuming a spectral index of $\alpha = -0.75$. Stellar masses and redshifts are determined using the optical-MIR photometry stellar synthesis library from Bruzual &

3. RESULTS

Charlot (2003), the results being the median from the likelihood distribution. The galaxies selected here have a $z = 0 - 4.5$ and a stellar mass of $10^8 \leq M_* \leq 10^{12}$.

AGNs are selected and removed using a recursive methodology. After correcting for mass and redshift biases within the data, they calculate $q_{\text{IR,peak}}$ which represents the mode of the radio detections. A histogram is created about the $q_{\text{IR,peak}}$ which has a main peak to the right and a secondary peak in the left (See Figure 10 in Delvecchio et al. (2021)). It is assumed that the main peak is due to SFGs and the secondary due to AGNs. Two Gaussians are then fitted about these two peaks representing the SFG and AGN populations respectively. This is done first by assuming the SFG histogram is symmetric, so they mirror the SFG histogram about its peak from right to left. All galaxies below 2σ of the SFG histogram are classified as AGNs and are removed. This corresponds to on average, 0.43 dex below q_{peak} .

This process is then repeated recursively until such time as the $q_{\text{IR,peak}}$ does not change between fits. As it happens, they find it is only necessary to run this process twice.

The recursive AGN selection method is conducted only on galaxies with $M_* > 10^{10.5}$. The bins of galaxies below this are largely incomplete and therefore do not represent a representative sample of the stellar masses. Using their two complete bins they find a $q_{\text{IR}} - z$ relationship of $q_{\text{IR}} \propto (1 + z)^{-0.055 \pm 0.018}$. Assuming that the remaining bins have the same slope of the $q_{\text{IR}} - z$ relationship, they extrapolate the recursive AGN removal method with the normalisation being left to vary. After this fit all galaxies below 0.43 dex of this best fit are identified as AGNs are removed.

As before, this process is repeated recursively until the median q_{IR} does not change between processes, outside of uncertainties.

Following this process, the authors fit a surface in the three-dimensional $rmq_{\text{IR}} - M_* - z$ space to find Equation 3.10. Two main findings of this paper was that q_{IR} does not evolve strongly with z , but does evolve with stellar mass.

Delvecchio et al. (2021) also compares with the results of Magnelli et al. (2015) and Delhaize et al. (2017). Following the same methods as outlined in these two papers (in particular AGN identification and removal), they find similar results with different data sets. This adds strong evidence that the tension between q'_{IR} s evolution (or lack thereof) with redshift is due to different AGN identification procedures.

In the yellow line shows the result from Bell (2003) which is $q_{\text{IR}} = 2.64 \pm 0.02$. The shaded yellow region shows the uncertainty from this result. Bell (2003) uses IR data from the Infrared Astronomical Satellite (IRAS) and radio data from the NRAO VLA Sky Survey (NVSS). This uses data from local SFGs ($z = 0$) and no stellar masses were estimated. AGNs have not been excluded from this sample, which makes it remarkable that the q_{IR} is so high. The result from Bell (2003) is cited in many papers as a standard result to which to compare.

Figure 3.11 allows for a four-way comparison of different q_{IR} results. From this figure, it is clear that the GAMA data, Bell (2003) data and SHARK data all agree in the $10^{10} - 10^{12} M_{\odot}$ range. As this is where the majority of the data from GAMA and Bell (2003) comes from, this indicates that SHARK can reproduce the observations that lead to this data. There is some

scatter from the SHARK data and the GAMA data, but that is to be expected.

There is very little GAMA data in mass ranges below $10^{10} - 10^{12} M_{\odot}$ and the data from Bell (2003) did not have stellar mass estimates, so comparisons here with SHARK are not meaningful. However, below $10^{10} M_{\odot}$, the SHARK q_{IR} drops off dramatically. The reason for this drop off, which will be discussed in depth in coming sections, is due to these low mass galaxies being no longer optically thick at UV wavelengths. In line with the calorimetric model, young massive stars produce UV radiation which is absorbed by dusty, molecular clouds in which these stars are formed and re-radiated in IR wavelengths. The key assumption here is that these clouds are totally optically thick to UV wavelengths. However for low mass galaxies, this assumption begins to fall away. The result is that these galaxies no longer produce the same amount of IR radiation due to star-formation.

Radio luminosities are unaffected by this; CCSNe will still accelerate cosmic rays into synchrotron radiation irrespective of the UV opacity of the galaxy.

It's for this reason why at these low mass ranges, SHARK no longer agrees with Bell (2003).

The striking feature of this Figure is the difference between the data from SHARK and Delvecchio et al. (2021). At no stellar mass does the slope of Delvecchio et al. (2021) agree with SHARK, though there is an intersection at $10^{9.5} M_{\odot}$. There are many reasons for this, which I will now discuss.

Firstly, Delvecchio et al. (2021) assumes that the slope of the $q_{\text{IR}} - z$ relation is the same for high mass and low mass galaxies when removing AGNs. As I show in later, this is not the case in SHARK. SHARK predicts that the slope of $q_{\text{IR}} - z$ is positive, but flattens out for $10^8 \leq M_{*} \leq 10^9 M_{\odot}$ and this trend continues, but in a less dramatic way for $10^9 M_{*} \leq 10^{10}$. SHARK does predict a relatively constant slope for the $q_{\text{IR}} - z$ relation for SFGs with stellar mass $10^{10} M_{*} \leq 10^{11}$ and $10^{11} M_{*} \leq 10^{12}$. This lends credence to the logic behind the assumption Delvecchio et al. (2021) made. This was based on the results from the bins $10^{10.5} M_{*} \leq 10^{11}$ and $10^{11} M_{*} \leq 10^{12}$ in Delvecchio et al. (2021) which showed little slope evolution like SHARK. Examining only these bins would lead to the assumption that the slope does not change.

The effect of this assumption is that many more SFGs are removed from the lower stellar mass bins in Delvecchio et al. (2021) than may be strictly necessary. If the observations were to be similar to the results from SHARK, then many of these lower mass galaxies would have a lower q_{IR} . Later, I also show that the distribution of SHARK galaxies in the $q_{\text{IR}} - M_{*}$ plane is bimodal. A relatively flat slope would more easily fit with the upper population of galaxies. Thus, when fitting the constant slope and removing all 0.43dex below this fit, there exists (at least in SHARK) SFGs that would be removed in this process. While other papers can attribute their evolution with $q_{\text{IR}} - z$ due to AGN identification process being not strict enough, perhaps the method used in Delvecchio et al. (2021) is too strict for low mass galaxies.

That being said, Shark may be over estimating the amount of SFGs at these masses. The proportion of galaxies which contain AGNs is high at low stellar masses (cite). So in that sense, the strength of these galaxies may be overstated.

The most credible explanation for while Delvecchio et al. (2021) (and indeed any other obser-

3. RESULTS

vational papers) do not predict that q_{IR} is so low at low stellar mass is because they would be difficult to detect. Low mass galaxies already have a lower luminosities and are therefore excluded from many flux limited surveys. Add to that that these galaxies are particularly IR faint, then the likelihood of a survey being able to detect a IR-faint, low mass galaxy is very slim. The radio component of such galaxies with also be faint, (though not as faint) so it would require the flux limits of two instruments being low enough to measure the radio and IR component of such a galaxy. This makes SHARK's prediction particularly difficult to confirm. A final point for why this difference exists is the possibility of new physics. Other papers such as Bell (2003) and Lacki et al. (2010) suggest conspiracies to explain FIRC. Such conspiracies are not included in SHARK as the physics behind them are not widely accepted and there is significant difficulty in modelling them on the scale of a SAM. However, if such a conspiracy is the reason behind Delvecchio et al. (2021) observations, then SHARK would not be able to reproduce the observational results that Delvecchio et al. (2021) found.

3.0.5 Evolution of q_{IR} with redshift

In this section, I weigh into the debate of evolution (or lack thereof) of q_{IR} with redshift. To do so, I consider the different populations of galaxies established thus far (all SHARK galaxies, SFGs and (U)LIRGs) and measure their q_{IR} at different snapshots of SHARK.

Figure 3.12 shows the evolution of q_{IR} with redshift for all SHARK galaxies and SFGs for different stellar mass bins. This is compared with results from Mao et al. (2011) and Delvecchio et al. (2021).

In the $8.0 \leq \log_{10}(M_*) < 9.0$ bin a relationship emerges with q_{IR} galaxies that is visually similar to the $q_{IR} - M_*$ evolution. Starting at about $q_{IR} \sim 2$, q_{IR} increases with redshift until it appears to asymptotically tend towards the result from Mao et al. (2011). This evolution is remarkable in that, compared with observational results that suggest that q_{IR} evolves with redshift, it is evolving, but in the wrong direction. This is seen in the significant disagreement that the results from SHARK has with Delvecchio et al. (2021). This evolution is seen in SFGs as well with both lines being nearly indistinguishable from each other.

Firstly, why is this evolution seen? It's not because of the model developed in the previous section of a birth cloud dominated galaxy having lower q_{IR} because of lower IR, rather it's likely the radio that has increased. With increasing redshift, SFR increases (See Figure 3.6). This increased SFR will directly increase the L_{rad} that is emitted from this galaxy. This can counteract the decrease in L_{IR} that is caused by the birth cloud dominated galaxies.

Secondly, why the big discrepancy with Delvecchio et al. (2021)? As discussed in section 3.0.4, the result from Delvecchio et al. (2021) finds the $q_{IR} - z$ slope for higher mass galaxies and extrapolates this to lower mass galaxies. This result from SHARK questions the validity of this assumption. From other panels, it is possible to see that this is not the case for SHARK galaxies. Assuming this slope leads to an over-zealous removal of lower mass galaxies with lower q_{IR} , mistaking them for AGNs. This means that the Delvecchio et al. (2021) will predict a higher IR

than what is seen in SHARK.

In the $9.0 \leq \log_{10}(M_*)10.0$ and $9.0 \leq \log_{10}(M_*)10.0$ panels show similar results, so I will discuss them both at the same time here. A similar relationship between q_{IR} and redshift is seen as in $8.0 \leq \log_{10}(M_*)9.0$, but to a less extent. At this stellar mass, galaxies are no longer birth cloud dominated, and their IR emission starts to increase as a result. For both the whole and SFG sample a slight increase in q_{IR} is seen reflecting, as seen in lower masses, the increase in SFR with redshift. Overall, q_{IR} is higher than at lower masses, indicating that the birth clouds and ISM are well mixed so the IR emission does not drop. This stellar mass bin has the best agreement with observations.

The final panel shows the only decoupling of SFGs and whole galaxy sample. In the definition of a SFG used in SHARK, the average SFR will be higher since all galaxies from -0.3 dex and above will be selected from the MS. In other mass bins, this has not made a material difference because galaxies of those masses do not vary from the galaxy as much MS, but in these mass bins, there is quite a bit of variance. Further, the MS fit is done using galaxies $9.0 \leq \log_{10}(M_*)10.0$, so it would be unreasonable to expect much deviation for those galaxies or those with stellar masses near it. But $11.0 \leq \log_{10}(M_*) \leq 12.0$ is two orders of magnitude away from the MS fit, so the MS fit starts to deviate from where the average galaxy lies on the SFR – M_* plane. Having a higher SFR means that the SFGs will have a higher radio emission. A high radio emission means they will have a lower q_{IR} .

It's also at this stellar mass bin that SHARK simply runs out of galaxies of this mass. Only bins with ten or more galaxies are plotted, so no meaningful relation can be seen for these large galaxies beyond $z \sim 4$.

Like the lowest mass bin, the results here disagree with the relation found in [Delvecchio et al. \(2021\)](#), but in the opposite direction; SHARK now predicts a higher q_{IR} than [Delvecchio et al. \(2021\)](#). This is true for both SFGs and the entire sample, even accounting for the SFR difference between the two. It's possible that AGN contamination in [Delvecchio et al. \(2021\)](#) is causing this difference.

Overall, Figure 3.12 finds a novel result that what is found in the literature. Mainly that q_{IR} does evolve with redshift, but it increases rather than decreases. However, the main driver of q_{IR} evolution is stellar mass. To some extent this confirms the hypothesis from [Delvecchio et al. \(2021\)](#), but in the opposite direction.

Figure 3.13 shows

Figure 3.13 shows the distribution of q_{IR} with stellar mass. It compares the distribution from SHARK as well as results from [Lo Faro et al. \(2015\)](#) and [Sargent et al. \(2010b\)](#). These are the same results that were plotted in Figure 3.3.

There are two important caveats with this plot; first is that the data from [Lo Faro et al. \(2015\)](#) is of individual galaxies, whereas the SHARK data is a population's mean and standard deviation. The line from [Sargent et al. \(2010b\)](#) shows the median value of $2.672^{+0.121}_{-0.121}$ which was found over a population of over 1000 ULIRGs.

The second caveat is that [Lo Faro et al. \(2015\)](#) and [Sargent et al. \(2010b\)](#) made no comparison

3. RESULTS

of q_{IR} vs. stellar mass, which is why both lines are set to flat. The purpose of including this data here is to act as a baseline from which I can compare the results from SHARK. The results from these papers agrees favourably with SHARK. Within the mass range of the [Lo Faro et al. \(2015\)](#), the SHARK model agrees with the almost all of the LIRG data.

Again, that there is scatter with the [Lo Faro et al. \(2015\)](#) data is not surprising; individual galaxies do exists outside of the median and $1 - \sigma$ scatter.

qir and extinction

qir vs. z

3.0.6 Number Counts

Lightcone

Number counts with z

Stellar Mass and SFR with z

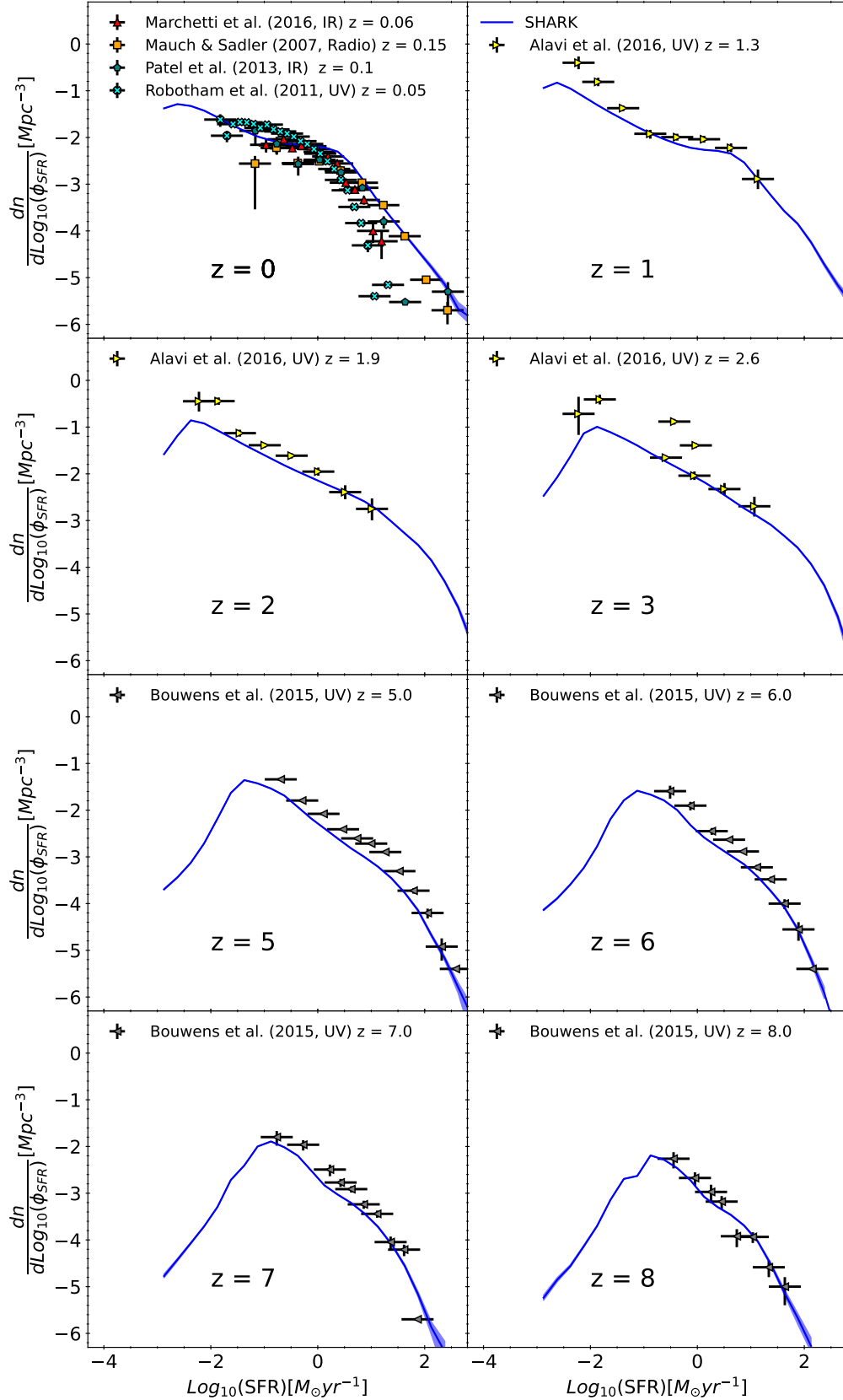


Figure 3.6: The SFR function over different redshift bins compared with observational data from Marchetti et al. (2016), Mauch & Sadler (2007), Patel et al. (2013), Robotham et al. (2011), Alavi et al. (2016) and Bouwens et al. (2015). as converted to SFR densities in Katsianis et al. (2017). The results listed in Appendix A of Katsianis et al. (2017) is plotted here. Like other plots, SHARK is shown in blue and the area represents the estimate of the $1 - \sigma$ from bootstrapping.

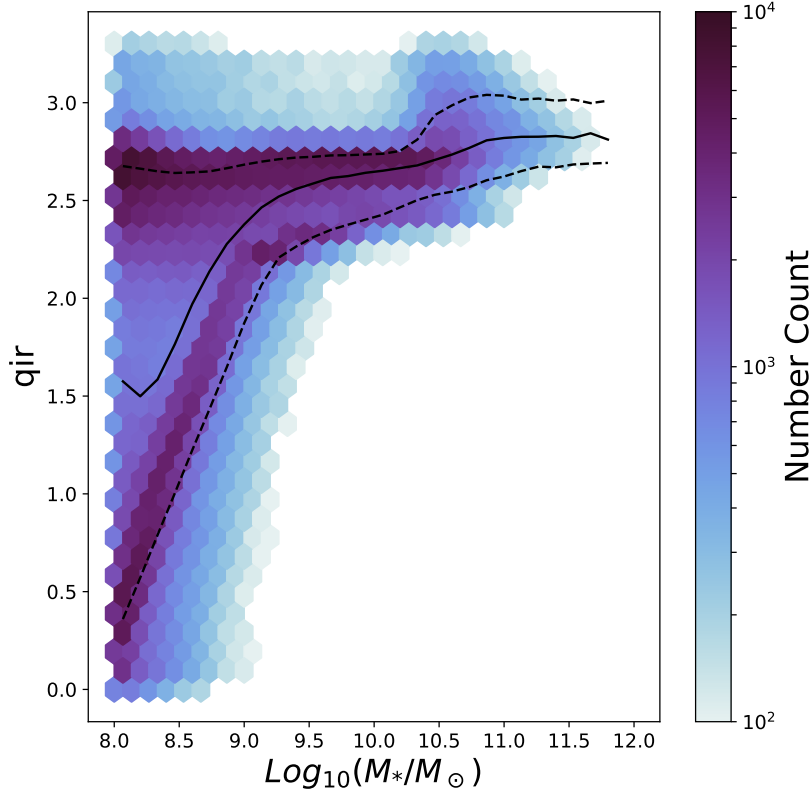


Figure 3.7: q_{IR} against M_* with coloured by number counts. The solid black line represents the median of the population and the dashed lines are $1 - \sigma$ uncertainty. Shown here are all SHARK galaxies with $10^8 M_\odot \leq M_* \leq 10^{12} M_\odot$ and $0 \leq q_{IR} \leq 3.3$ at $z = 0$. Only cells with more than 100 galaxies are displayed. Above $10^{10} M_\odot$, there is a single population of galaxies centered around q_{IR} 2.7 with no evolution evident. Below this there's evidence of two populations: one centered around q_{IR} 2.7 and a second that diverges from this population to a lower q_{IR} 0.5. There is evidence of evolution with M_* , but in the opposite way that [Delvecchio et al. \(2021\)](#) found. The colour map is from the package CMOCEAN ([Thyng et al. 2016](#)).

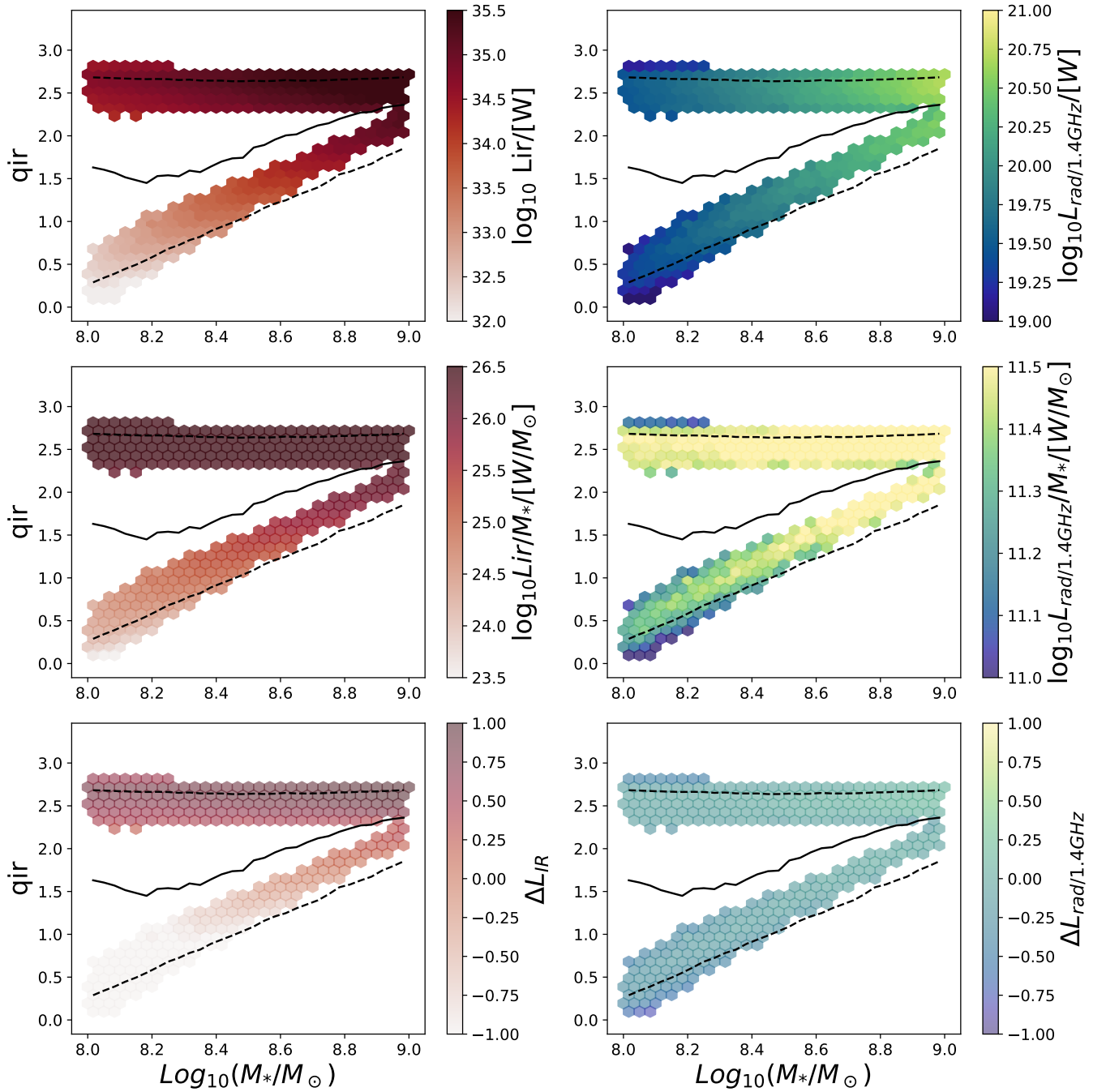


Figure 3.8: q_{IR} against M_* coloured by median IR luminosities (left column) and median radio luminosities (right column) properties. These plots focus in on masses $8_\odot \leq \log_{10}(M_*) \leq 9$ at $z = 0$. Only cells with 500 galaxies are shown here. As in Figure 3.7, the solid black line is the median of the population and the dashed lines represent $1 - \sigma$ uncertainty. The top row shows actual IR and radio luminosities in W and W respectively. The second shows IR/M_* and $Radio/M_*$ to remove any evolution the luminosities can have with M_* . The bottom plots show ΔL_{IR} and $\Delta L_{rad/1.4GHz}$ where this is the difference between the population and the median luminosity/ M_* . This Figure shows that while both L_{IR} and $L_{rad,1.4GHz}$ decrease in this second population, L_{IR} decreases more leading to the decline in q_{IR} . The colour maps are from the package CMOCEAN (Thyng et al. 2016).

3. RESULTS

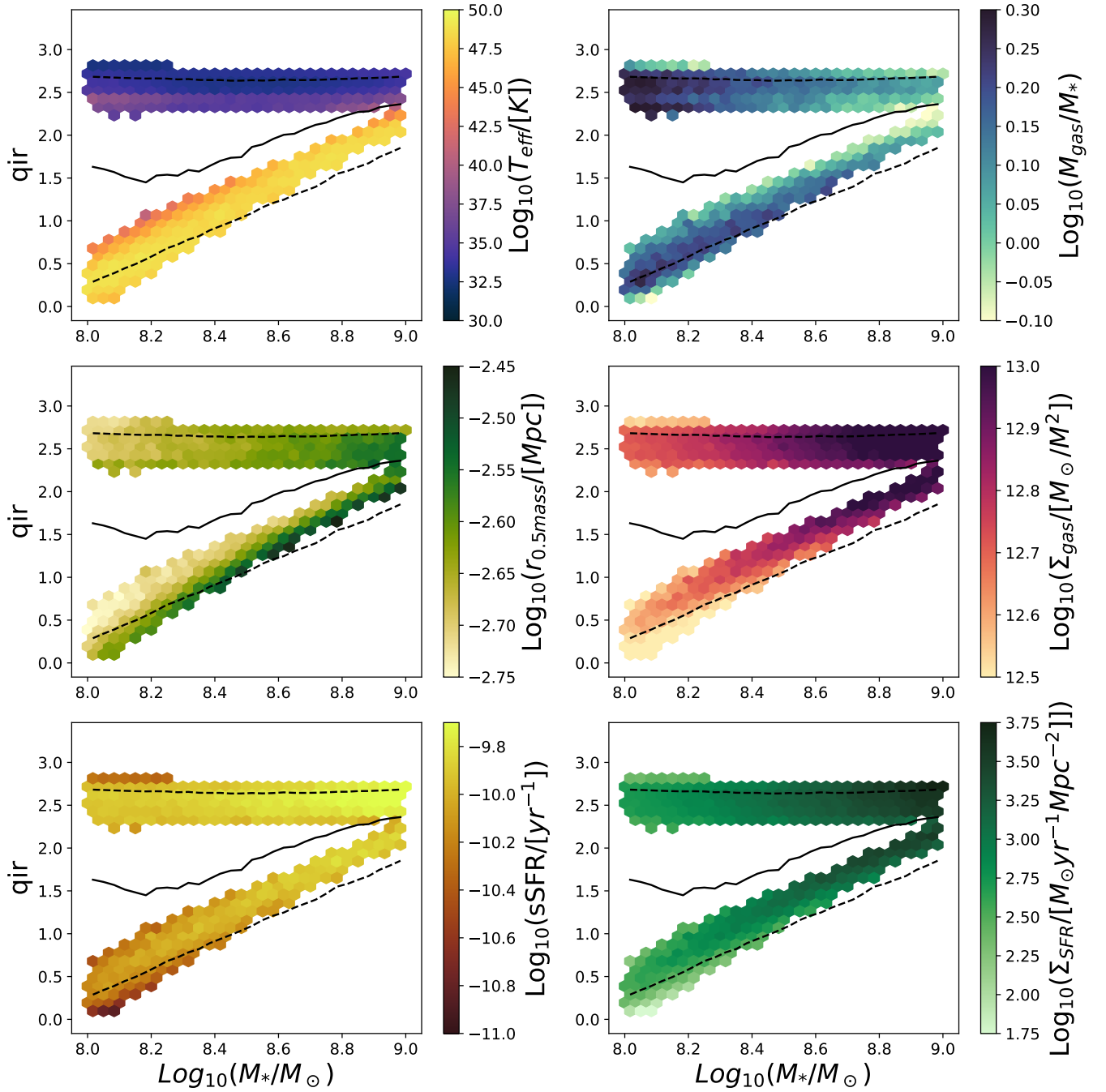


Figure 3.9: q_{IR} against M_* coloured a variety of properties. These plots focus in on masses $8_\odot \leq \log_{10}(M_*) \leq 9$ at $z = 0$. As in Figure 3.7, the solid black line is the median of the population and the dashed lines represent $1 - \sigma$ uncertainty. Only cells with 500 galaxies are shown here. The upper left plot is coloured by effective dust temperature (T_{eff}). The upper right plot is coloured by the total gas mass (M_{gas}). The middle left plot is coloured by the half-mass radius of the disk ($r_{0.5\text{mass}}$). The middle right plot is coloured by gas surface density (Σ_{gas}). The lower left plot is coloured by specific star-formation rate (sSFR). The lower right plot is coloured by SFR surface density (Σ_{SFR}). The colour maps are from the package CMOCEAN (Thyng et al. 2016).

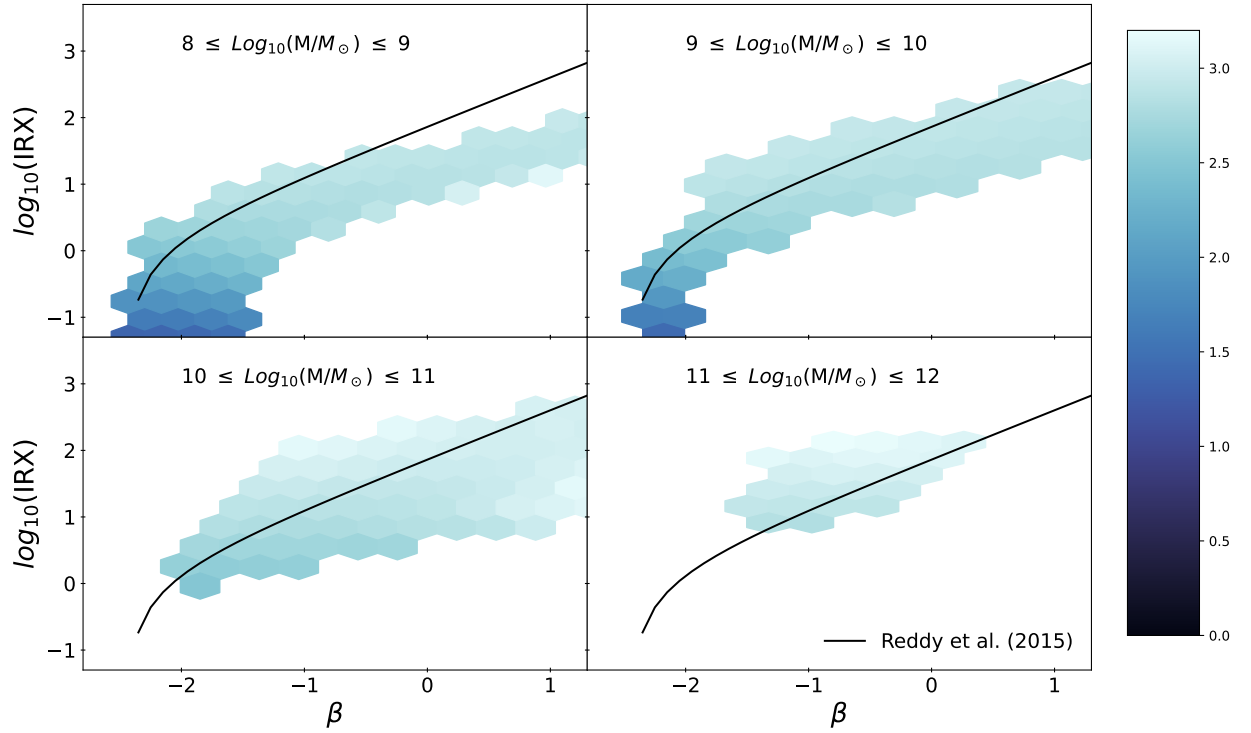


Figure 3.10: The IRX- β plane for different stellar masses coloured by the median q_{IR} of the bin. A subset of galaxies from SHARK are selected for this plot (See text) at $z = 0$. This is compared with the IRX- β plane as found using dust attenuation curves found in Reddy et al. (2015). Only cells with more than 100 galaxies within are shown. The colour map is from the package CMOCEAN (Thyng et al. 2016).

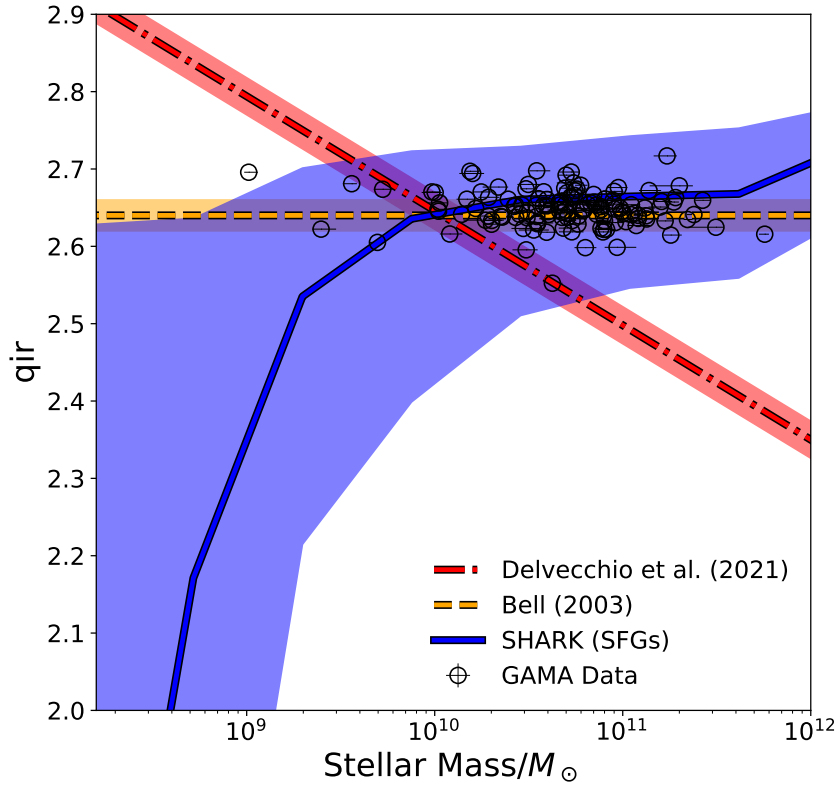


Figure 3.11: q_{ir} vs. total stellar mass compared with observational data of individual galaxies from the GAMA survey. These are the same galaxies as in Fig. ???. The blue region shows galaxies from SHARK, with the thick line being the median result and the shaded blue region showing $1 - \sigma$ uncertainty. The red dot-dashed line shows the q_{ir} vs. total stellar mass relationship found in Delvecchio et al. (2021) (Fig. 14 in that paper). The orange dashed line shows the constant q_{ir} found in Bell (2003).

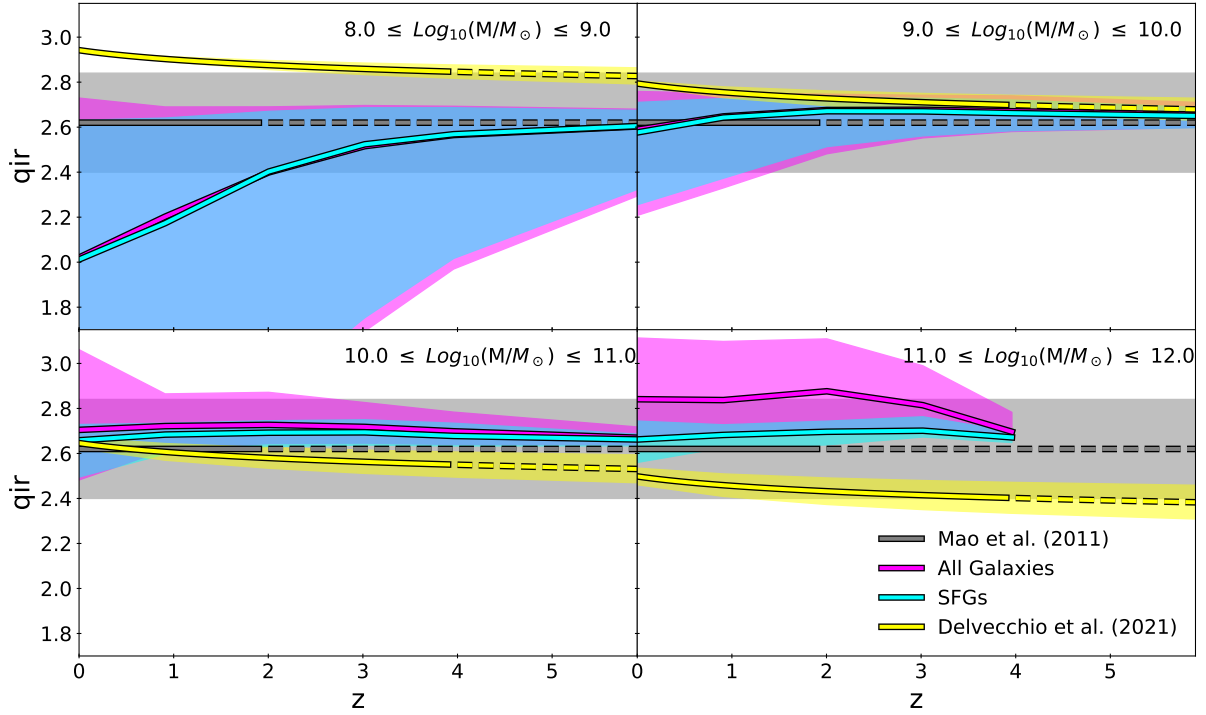


Figure 3.12: q_{IR} vs. z for different stellar mass bins for all galaxies in SHARK (shown in magenta) and those classified as SFGs (shown in cyan). As before, the thick magenta/cyan lines represent the median of that particular redshift bin and the shaded area represents $1 - \sigma$ uncertainty. The grey line represents the result from Mao et al. (2011) (2.620.22) with the grey shaded area representing the uncertainty found in that relation. Mao et al. (2011) only observed out to $z = 2$, so after this redshift, this result is a projection, which is indicated by the dashed line. The yellow line shows the result from Delvecchio et al. (2021) as defined in Equation 3.10. Delvecchio et al. (2021) only included observations to $z = 4.5$, so after this point the relation is extrapolated which is indicated using a dashed line.

3. RESULTS

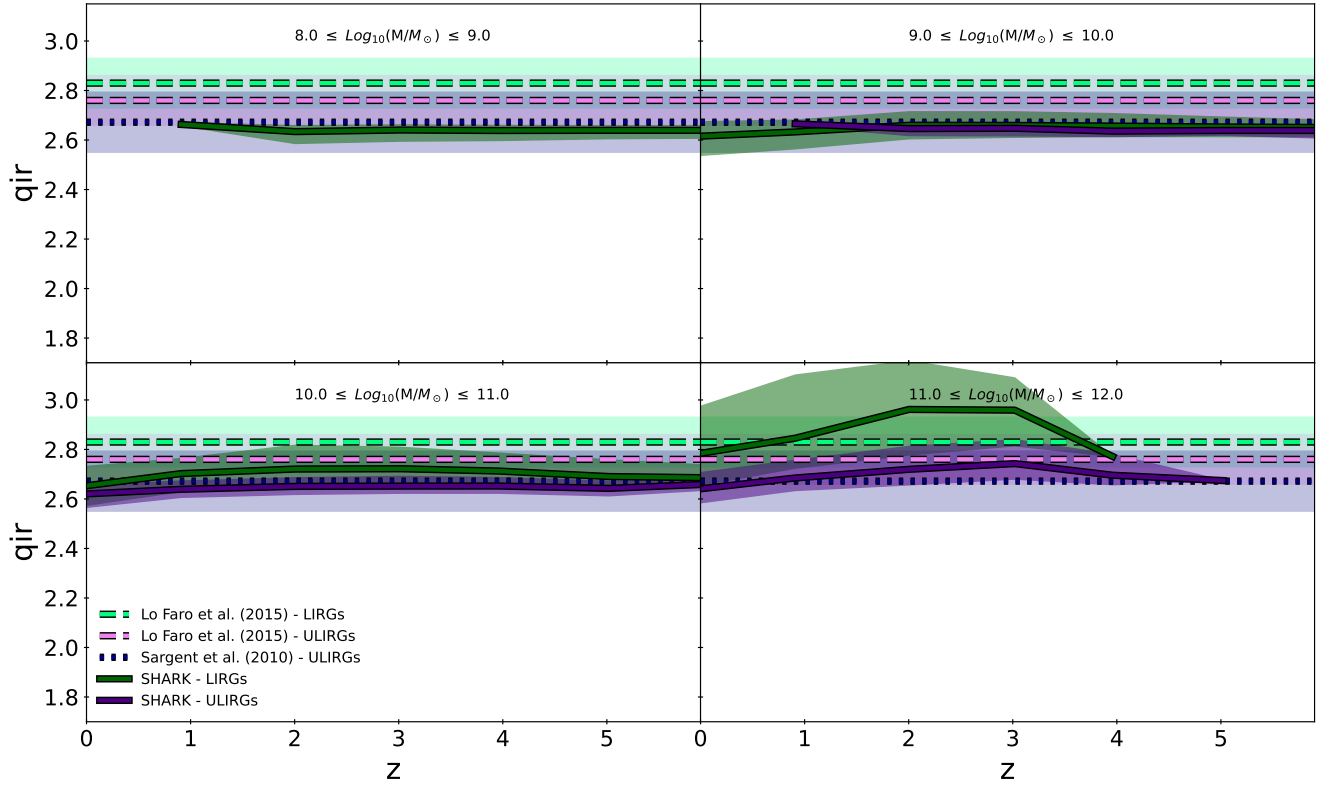


Figure 3.13: q_{IR} vs. z for different stellar mass bins for (U)LIRGs where LIRGs are shown in green and ULIRGs are shown in purple. As before, the thick line shows the median and the shaded area shows the $1 - \sigma$ uncertainty. This is compared with results from [Lo Faro et al. \(2015\)](#) and [Sargent et al. \(2010b\)](#). The galaxies used here are the same as the as in Figure 3.3.

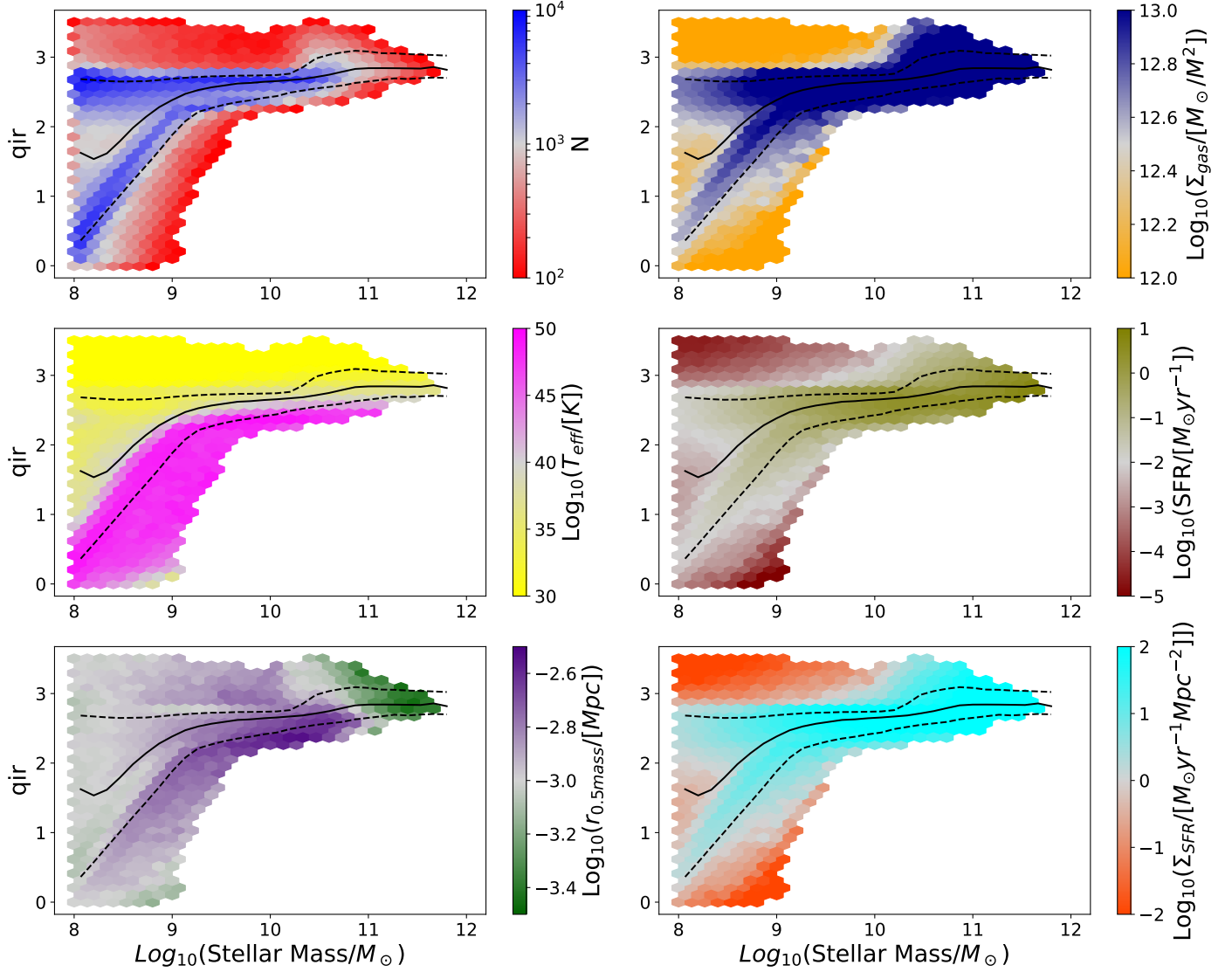


Figure 3.14: qir vs. total stellar mass coloured by different parameters. Upper left most panel shows number counts. Upper right panel shows coloured by effective dust temperature. Lower left panel shows coloured by half mass radius and lower right panel shows coloured by gas surface density. Solid black line shows the median qir evolution with total stellar mass and the dashed black lines show $1 - \sigma$ uncertainty.

3. RESULTS

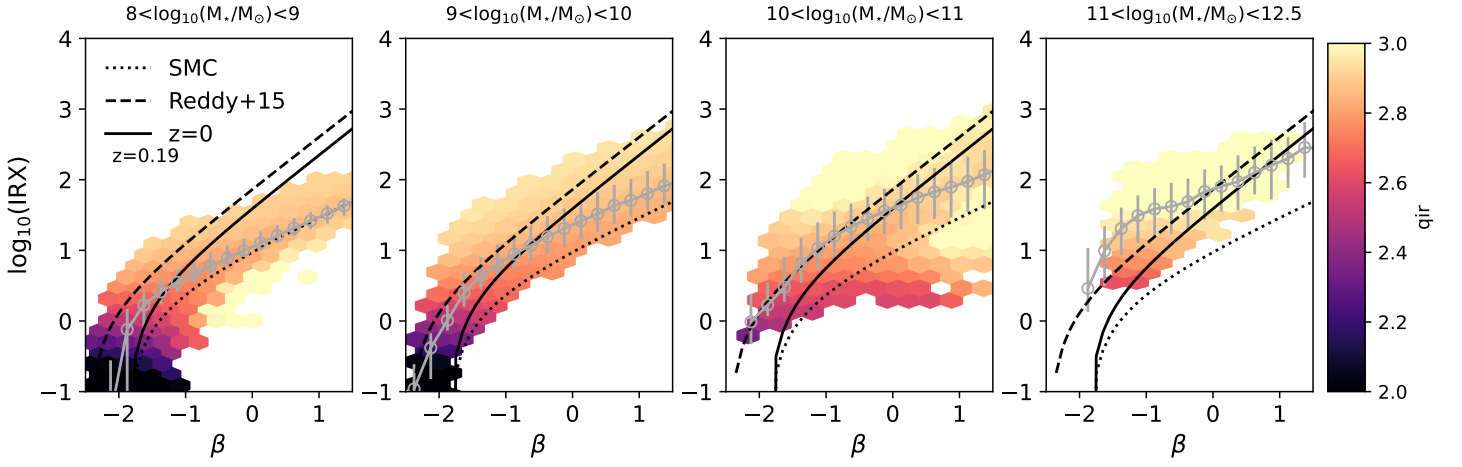


Figure 3.15: IRX-Beta function plot at $z = 0.19$ coloured by q_{ir} .

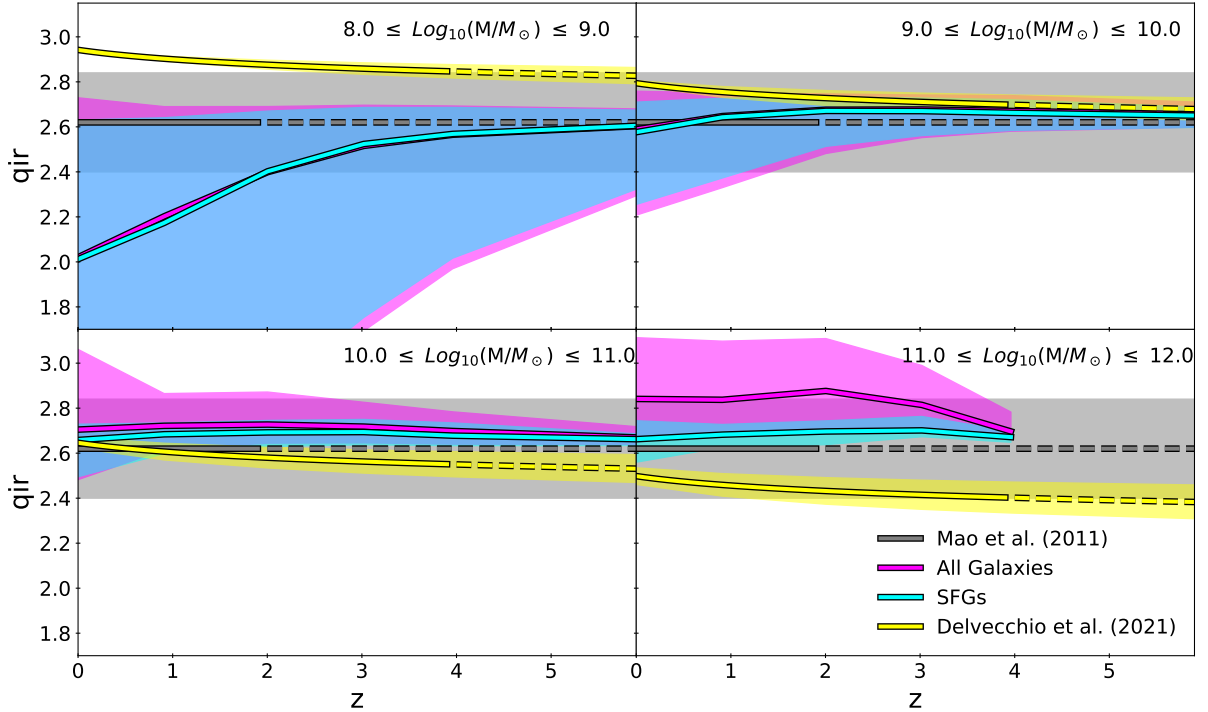


Figure 3.16: q_{ir} vs. z for different stellar mass bins. Solid line shows the median and the shaded regions show the $1 - \sigma$ uncertainty.

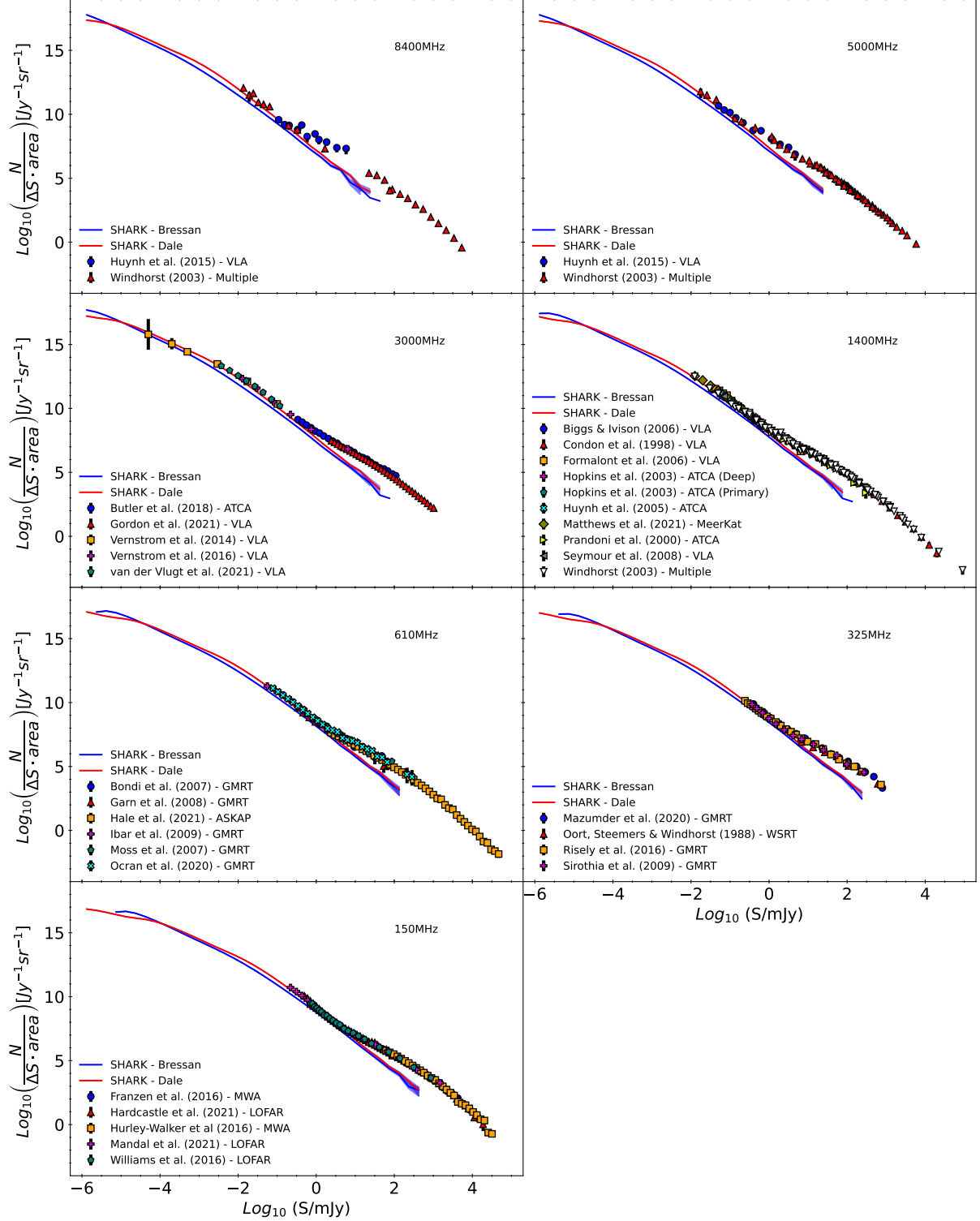


Figure 3.17: The number counts per redshift for different radio frequencies for all galaxies with $|rmS| > 10^{-2} \text{ mJy}$. Solid lines are the median line and the shaded area represents $1 - \sigma$ estimated using bootstrapping.

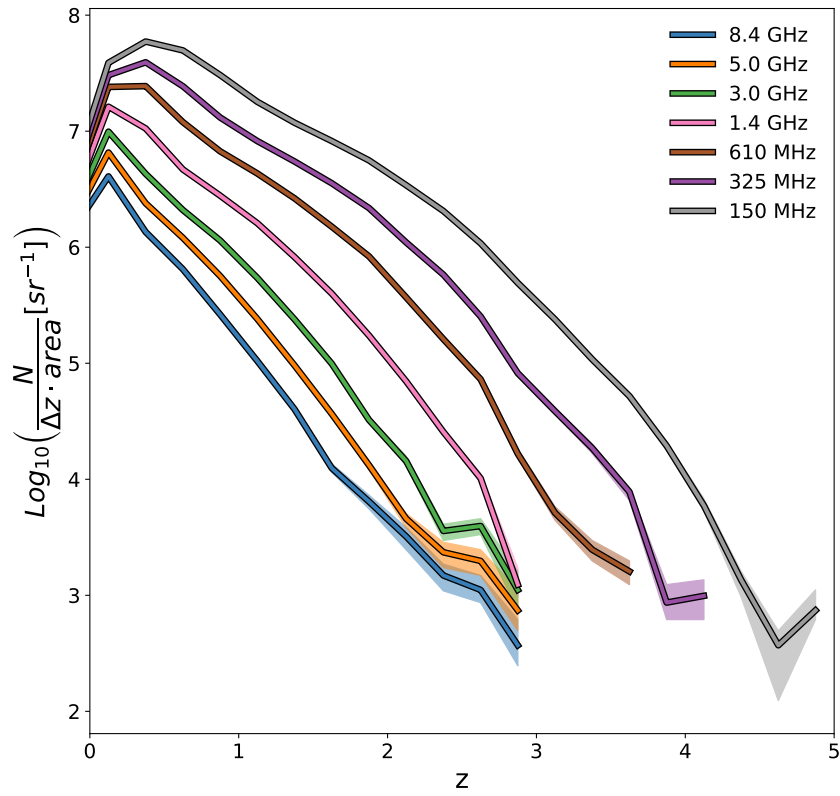


Figure 3.18: The number counts per redshift for different radio frequencies for all galaxies with $S > 10^{-2} \text{ mJy}$. Solid lines are the median line and the shaded area represents $1 - \sigma$ estimated using bootstrapping.

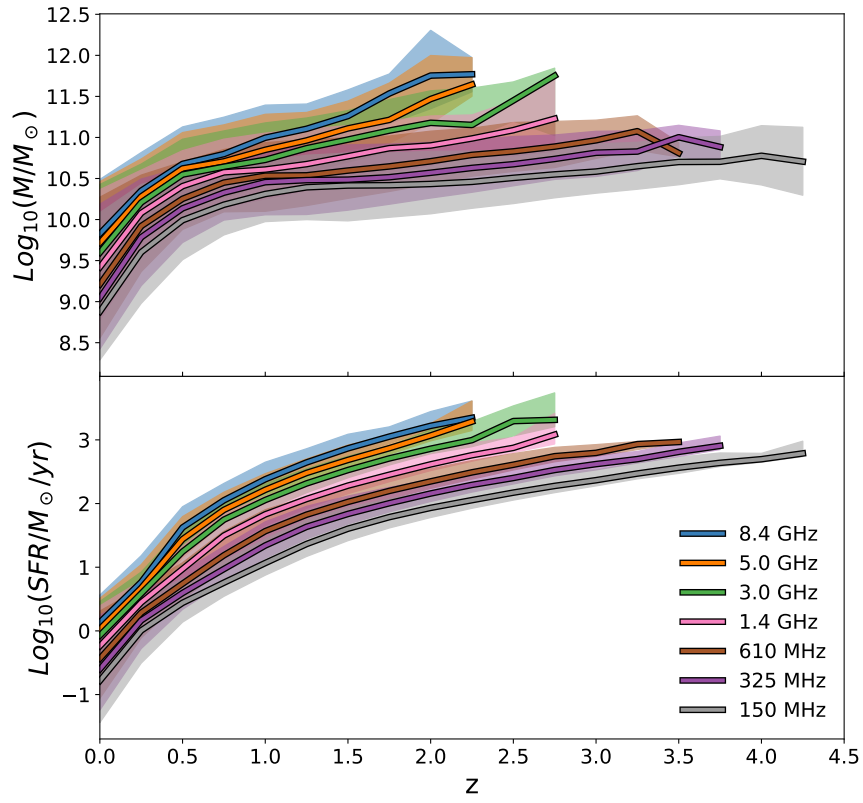


Figure 3.19: Upper panel shows the median total stellar mass of all galaxies with $S > 10^{-2} \text{ mJy}$ for different radio frequencies. Shaded area represents $1 - \sigma$ region. Lower panel shows the same but median SFR.

Chapter 4

Discussion

4.1 TBD

TEXT

Chapter 5

Conclusion

TBD

Chapter 6

Future Work

TBD

References

- Alavi A., et al., 2016, *The Astrophysical Journal*, 832, 56
- Algera H., et al., 2020, *The Astrophysical Journal*, 903, 138
- Anderson L., Bania T., Jackson J., Clemens D., Heyer M., Simon R., Shah R., Rathborne J., 2009, *The Astrophysical Journal Supplement Series*, 181, 255
- Ando S., Sato K., Totani T., 2003, *Astroparticle Physics*, 18, 307
- Appleton P., et al., 2004, *The Astrophysical Journal Supplement Series*, 154, 147
- Baldwin J. A., Phillips M. M., Terlevich R., 1981, *Publications of the Astronomical Society of the Pacific*, 93, 5
- Baugh C., Lacey C. G., Frenk C., Granato G., Silva L., Bressan A., Benson A., Cole S., 2005, *Monthly Notices of the Royal Astronomical Society*, 356, 1191
- Bell E. F., 2003, *The Astrophysical Journal*, 586, 794
- Bellstedt S., et al., 2020, *Monthly Notices of the Royal Astronomical Society*, 496, 3235
- Berkhuijsen E., 1984, *Astronomy and Astrophysics*, 140, 431
- Bolton A. S., et al., 2012, *The Astronomical Journal*, 144, 144
- Bolzonella M., Miralles J.-M., Pelló R., 2000, *Arxiv preprint astro-ph/0003380*
- Bonato M., Prandoni I., De Zotti G., Brienza M., Morganti R., Vaccari M., 2021a, *Monthly Notices of the Royal Astronomical Society*, 500, 22
- Bonato M., et al., 2021b, *Astronomy & Astrophysics*, 656, A48
- Bourne N., Dunne L., Ivison R., Maddox S., Dickinson M., Frayer D., 2011, *Monthly Notices of the Royal Astronomical Society*, 410, 1155
- Bouwens R. J., et al., 2015, *The Astrophysical Journal*, 803, 34
- Bressan A., Silva L., Granato G. L., 2002, *Astronomy & Astrophysics*, 392, 377

REFERENCES

- Bruzual G., Charlot S., 2003, *Monthly Notices of the Royal Astronomical Society*, 344, 1000
- Butler A., et al., 2018, *Astronomy & Astrophysics*, 620, A16
- Butler A., Huynh M., Kapińska A., Delvecchio I., Smolčić V., Chiappetti L., Koulouridis E., Pierre M., 2019, *Astronomy & Astrophysics*, 625, A111
- Calzetti D., Kinney A. L., Storchi-Bergmann T., 1994, *The astrophysical journal*. Chicago. Vol. 429, no. 2, pt. 1 (July 1994), p. 582-601
- Camps P., Trayford J. W., Baes M., Theuns T., Schaller M., Schaye J., 2016, *Monthly Notices of the Royal Astronomical Society*, 462, 1057
- Cañas R., Elahi P. J., Welker C., Lagos C. d. P., Power C., Dubois Y., Pichon C., 2019, *Monthly Notices of the Royal Astronomical Society*, 482, 2039
- Cappellaro E., Turatto M., 2001, in , *The influence of binaries on stellar population studies*. Springer, pp 199–214
- Chabrier G., 2003, *Publications of the Astronomical Society of the Pacific*, 115, 763
- Charlot S., Fall S. M., 2000, *The Astrophysical Journal*, 539, 718
- Chauhan G., Lagos C. d. P., Obreschkow D., Power C., Oman K., Elahi P. J., 2019, *Monthly Notices of the Royal Astronomical Society*, 488, 5898
- Condon J., 1992, *Annual review of astronomy and astrophysics*, 30, 575
- Condon J. J., Ransom S. M., 2016, *Essential radio astronomy*. Vol. 2, Princeton University Press
- Cowley W. I., Lacey C. G., Baugh C. M., Cole S., Frenk C. S., Lagos C. d. P., 2019, *Monthly Notices of the Royal Astronomical Society*, 487, 3082
- Cutri R. M., Huchra J. P., Low F. J., Brown R. L., Vanden Bout P. A., 1994, *The Astrophysical Journal*, 424, L65
- Dale D. A., Helou G., Contursi A., Silbermann N. A., Kolhatkar S., 2001, *The Astrophysical Journal*, 549, 215
- Dale D. A., Helou G., Magdis G. E., Armus L., Díaz-Santos T., Shi Y., 2014, *The Astrophysical Journal*, 784, 83
- Davies L. J., et al., 2017, *Monthly Notices of the Royal Astronomical Society*, 466, 2312
- De Jong T., Klein U., Wielebinski R., Wunderlich⁹ E., 1985, *Astron. Astrophys*, 147, L6
- Delhaize J., et al., 2017, *Astronomy & Astrophysics*, 602, A4

- Delvecchio I., et al., 2021, *Astronomy & Astrophysics*, 647, A123
- Donley J., Rieke G., Rigby J., Pérez-González P., 2005, *The Astrophysical Journal*, 634, 169
- Draine B., Anderson N., 1985, *The Astrophysical Journal*, 292, 494
- Driver S. P., et al., 2022, , 513, 439
- Duncan K. J., Shivaee I., Shapley A. E., Reddy N. A., Mobasher B., Coil A. L., Kriek M., Siana B., 2020, *Monthly Notices of the Royal Astronomical Society*, 498, 3648
- Désert F.-X., Boulanger F., Puget J.-L., 1990, *Astronomy and Astrophysics*, 237, 215
- Elahi P. J., Welker C., Power C., Lagos C. d. P., Robotham A. S., Cañas R., Poulton R., 2018, *Monthly Notices of the Royal Astronomical Society*, 475, 5338
- Elahi P. J., Cañas R., Poulton R. J., Tobar R. J., Willis J. S., Lagos C. d. P., Power C., Robotham A. S., 2019a, *Publications of the Astronomical Society of Australia*, 36, e021
- Elahi P. J., Poulton R. J., Tobar R. J., Cañas R., Lagos C. d. P., Power C., Robotham A. S., 2019b, *Publications of the Astronomical Society of Australia*, 36, e028
- Fadda D., et al., 2010, *The Astrophysical Journal*, 719, 425
- Gehrels N., 1986, *The Astrophysical Journal*, 303, 336
- Giulietti M., et al., 2022, *Monthly Notices of the Royal Astronomical Society*, 511, 1408
- Heger A., Fryer C. L., Woosley S. E., Langer N., Hartmann D. H., 2003, *The Astrophysical Journal*, 591, 288
- Helou G., Soifer B., Rowan-Robinson M., 1985, *The Astrophysical Journal*, 298, L7
- Hopkins A. M., et al., 2003, *The Astrophysical Journal*, 599, 971
- Ivison R. J., et al., 2010a, *Monthly Notices of the Royal Astronomical Society*, 402, 245
- Ivison R., et al., 2010b, *Astronomy & Astrophysics*, 518, L31
- Jarvis M. J., et al., 2010, *Monthly Notices of the Royal Astronomical Society*, 409, 92
- Jin S., et al., 2018, *The Astrophysical Journal*, 864, 56
- Katsianis A., et al., 2017, *Monthly Notices of the Royal Astronomical Society*, 472, 919
- Kennicutt Jr R. C., 1998, *The astrophysical journal*, 498, 541
- Kreckel K., et al., 2013, *The Astrophysical Journal*, 771, 62

REFERENCES

- Kregel M., Van Der Kruit P. C., Grijs R. d., 2002, *Monthly Notices of the Royal Astronomical Society*, 334, 646
- Krumholz M. R., 2014, *Physics Reports*, 539, 49
- Krumholz M. R., McKee C. F., Tumlinson J., 2009, *The Astrophysical Journal*, 699, 850
- Lacey C., Baugh C., Frenk C., Silva L., Granato G., Bressan A., 2008, *Monthly Notices of the Royal Astronomical Society*, 385, 1155
- Lacey C. G., et al., 2016, *Monthly Notices of the Royal Astronomical Society*, 462, 3854
- Lacki B. C., Thompson T. A., Quataert E., 2010, *The Astrophysical Journal*, 717, 1
- Lagache G., Puget J.-L., Dole H., 2005, *Annu. Rev. Astron. Astrophys.*, 43, 727
- Lagos C. d. P., Tobar R. J., Robotham A. S., Obreschkow D., Mitchell P. D., Power C., Elahi P. J., 2018, *Monthly Notices of the Royal Astronomical Society*, 481, 3573
- Lagos C. d. P., et al., 2019, *Monthly Notices of the Royal Astronomical Society*, 489, 4196
- Li A., 2020, *Nature Astronomy*, 4, 339
- Lo Faro B., et al., 2013, *The Astrophysical Journal*, 762, 108
- Lo Faro B., Silva L., Franceschini A., Miller N., Efstathiou A., 2015, *Monthly Notices of the Royal Astronomical Society*, 447, 3442
- Magnelli B., et al., 2015, *Astronomy & Astrophysics*, 573, A45
- Mao M. Y., Huynh M. T., Norris R. P., Dickinson M., Frayer D., Helou G., Monkiewicz J. A., 2011, *Proceedings of the International Astronomical Union*, 7, 404
- Marchetti L., et al., 2016, *Monthly Notices of the Royal Astronomical Society*, 456, 1999
- Mauch T., Sadler E. M., 2007, *Monthly Notices of the Royal Astronomical Society*, 375, 931
- Messias H., Afonso J., Salvato M., Mobasher B., Hopkins A. M., 2012, *The Astrophysical Journal*, 754, 120
- Mezger P., Henderson A., 1967, *The Astrophysical Journal*, 147, 471
- Molnár D. C., et al., 2021, *Monthly Notices of the Royal Astronomical Society*, 504, 118
- Nomoto K., 1984, *The Astrophysical Journal*, 277, 791
- Norris R. P., et al., 2006, *The Astronomical Journal*, 132, 2409
- Novak M., et al., 2017, *Astronomy & Astrophysics*, 602, A5

- Obi I., et al., 2017, arXiv preprint arXiv:1702.02230
- Ocran E., Taylor A., Vaccari M., Ishwara-Chandra C., Prandoni I., Prescott M., Mancuso C., 2019, arXiv preprint arXiv:1912.00934
- Ocran E., Taylor A., Vaccari M., Ishwara-Chandra C., Prandoni I., 2020, Monthly Notices of the Royal Astronomical Society, 491, 1127
- Omar A., Paswan A., 2018, Monthly Notices of the Royal Astronomical Society, 477, 3552
- Oster L., 1961, Reviews of Modern Physics, 33, 525
- Patel H., Clements D., Vaccari M., Mortlock D., Rowan-Robinson M., Pérez-Fournon I., Afonso-Luis A., 2013, Monthly Notices of the Royal Astronomical Society, 428, 291
- Pavlović M., 2021, Serbian Astronomical Journal, pp 15–27
- Planck Collaboration Ade P. A., et al., 2016, Astronomy & Astrophysics, 594, A13
- Read S. C., et al., 2018, Monthly Notices of the Royal Astronomical Society, 480, 5625
- Reddy N. A., et al., 2015, The Astrophysical Journal, 806, 259
- Reddy N. A., et al., 2018, , 853, 56
- Robotham A. S., et al., 2011, Monthly Notices of the Royal Astronomical Society, 416, 2640
- Robotham A., Bellstedt S., Lagos C. d. P., Thorne J., Davies L., Driver S., Bravo M., 2020, Monthly Notices of the Royal Astronomical Society, 495, 905
- Rubin R. H., 1968, The Astrophysical Journal, 154, 391
- Salpeter E. E., 1955, The Astrophysical Journal, 121, 161
- Sargent M. T., et al., 2010a, The Astrophysical Journal Supplement Series, 186, 341
- Sargent M. T., et al., 2010b, The Astrophysical Journal Letters, 714, L190
- Schober J., Sargent M., Klessen R., Schleicher D., 2022, arXiv preprint arXiv:2210.07919
- Seymour N., et al., 2008, Monthly Notices of the Royal Astronomical Society, 386, 1695
- Shao L., Koribalski B. S., Wang J., Ho L. C., Staveley-Smith L., 2018, Monthly Notices of the Royal Astronomical Society, 479, 3509
- Silva L., Granato G. L., Bressan A., Danese L., 1998, The Astrophysical Journal, 509, 103
- Smith D., et al., 2014, Monthly Notices of the Royal Astronomical Society, 445, 2232
- Smolčić V., et al., 2008, The Astrophysical Journal Supplement Series, 177, 14

REFERENCES

- Smolčić V., et al., 2017, *Astronomy & Astrophysics*, 602, A1
- Solarz A., Pollo A., Bilicki M., Pepiak A., Takeuchi T. T., Piatek P., 2019, *Publications of the Astronomical Society of Japan*, 71, 28
- Somerville R. S., Gilmore R. C., Primack J. R., Domínguez A., 2012, *Monthly Notices of the Royal Astronomical Society*, 423, 1992
- Strömgren B., 2013, in , *A Source Book in Astronomy and Astrophysics, 1900–1975*. Harvard University Press, pp 588–592
- Thomson A., et al., 2014, *Monthly Notices of the Royal Astronomical Society*, 442, 577
- Thyng K. M., Greene C., Hetland R., Zimmerle H., DiMarco S., 2016, *Oceanography*, 29
- Tran Q., et al., 2001, *The Astrophysical Journal*, 552, 527
- Trayford J. W., et al., 2017, *Monthly Notices of the Royal Astronomical Society*, 470, 771
- Trayford J. W., Lagos C. d. P., Robotham A. S., Obreschkow D., 2019, *arXiv preprint arXiv:1908.08956*
- Trčka A., et al., 2020, *Monthly Notices of the Royal Astronomical Society*, 494, 2823
- Trouille L., Barger A., Tremonti C., 2011, *The Astrophysical Journal*, 742, 46
- Tsai C.-W., et al., 2015, *The Astrophysical Journal*, 805, 90
- Tsujimoto T., Yoshii Y., Nomoto K., Matteucci F., Thielemann F.-K., Hashimoto M., 1997, *The Astrophysical Journal*, 483, 228
- Van Der Kruit P., 1973, *Astronomy and Astrophysics*, 29, 263
- Van den Heuvel E., Yoon S.-C., 2007, *Astrophysics and Space Science*, 311, 177
- Van der Kruit P., 1971, *Astronomy and Astrophysics*, Vol. 15, p. 110-122, 15, 110
- Vazdekis A., Koleva M., Ricciardelli E., Röck B., Falcón-Barroso J., 2016, *Monthly Notices of the Royal Astronomical Society*, 463, 3409
- Vega O., Silva L., Panuzzo P., Bressan A., Granato G., Chavez M., 2005, *Monthly Notices of the Royal Astronomical Society*, 364, 1286
- Völk H., 1989, *Astronomy and Astrophysics*, 218, 67
- Vollmer B., Soida M., Dallant J., 2022, *Astronomy & Astrophysics*, 667, A30
- Yun M., Carilli C., 1999, *Science with the Atacama Large Millimeter Array (ALMA)*, p. 78
- Yun M. S., Reddy N. A., Condon J., 2001, *The Astrophysical Journal*, 554, 803

TEXT